Discover Environment

Research

Development of novel nanocellulose based biofunctional materials from *Raphia farinifera* inflorescence with enhanced structural properties for high efficiency removal of hazardous organic contaminants from water

Chukwuebuka Gabriel Eze[2] · Emmanuel Agboeze[1] · I. P. Udeozo[1] · Vitus Anayo Ofordile[3] · Henry Okechukwu Agboeze[1]

Received: 21 July 2025 / Accepted: 18 November 2025
Published online: 23 November 2025
© The Author(s) 2025 OPEN

Abstract
This study evaluated the potential of biosorbents derived from *Raphia farinifera* inflorescence for the removal of atrazine from water. Raw (RFI-RAW), cellulose (RFI-C), nanocellulose (RFI-NCC), and xanthated nanocellulose (RFI-NCC-Xan) biosorbents were prepared and characterized using FTIR, SEM, and BET analyses. Batch adsorption experiments were conducted under varying conditions of pH, adsorbent dosage, initial concentration, contact time, and temperature. RFI-NCC-Xan achieved a maximum removal efficiency of 99.71% at pH 6, 40 °C, and an optimum contact time of 80 min, while RFI-C exhibited the highest adsorption capacity under Langmuir isotherm fitting ($q_m = 99.78$ mg/g). Non-linear isotherm models provided superior fits compared with linear forms, with R^2 values of 0.942–0.996 and RMSE < 0.012, confirming the suitability of Langmuir and Sips models. Kinetic data were best described by the pseudo-second-order model, with calculated and experimental adsorption capacities in close agreement (q_e,exp = 9.82 mg/g; q_e,calc = 9.74 mg/g for RFI-NCC-Xan). Thermodynamic evaluation from both linear and non-linear Van't Hoff analysis indicated that the adsorption was spontaneous ($\Delta G° = -1.34$ to -6.27 kJ mol^{-1} at 298 K) and endothermic, with $\Delta H°$ values ranging from +94.7 to +185.3 kJ·mol^{-1} depending on the biosorbent. Non-linear analysis provided more consistent $\Delta H°$ and $\Delta S°$ estimates, confirming the energetic favorability and entropy-driven nature of the process. Regeneration studies showed that RFI-NCC-Xan retained 81.59% efficiency after three cycles using 0.1 M NaOH, highlighting its stability and reusability. Application to real wastewater from Aninri, Enugu State, Nigeria, demonstrated > 93% atrazine removal during both dry and wet seasons. These findings establish *Raphia farinifera*-based biosorbents as cost-effective, renewable materials with strong potential for agricultural water treatment and sustainable herbicide remediation.

Keywords *Raphia farinifera* · Agro-waste valorization · Adsorption · Nanocrystalline cellulose · Waste water treatment · Atrazine herbicides

✉ Emmanuel Agboeze, emmanuel.agboeze@gmail.com; emmanuel.agboeze@esut.edu.ng | [1]Department of Science Laboratory Technology (Biochemistry Option), University of Nigeria Nsukka, Nsukka, Enugu State, Nigeria. [2]Department of Industrial Chemistry, Enugu State University of Science and Technology, Agbani, Enugu State, Nigeria. [3]Federal Ministry of Innovation, Science and Technology, Abuja, Nigeria.

1 Introduction

Herbicide pollution remains a persistent environmental concern due to its toxicity, resistance to degradation, and potential to bioaccumulate, causing severe ecological and health impacts. In Nigeria and other developing countries, the increasing application of herbicides has led to contamination of soil, surface water, and groundwater, raising public health risks. Atrazine, a chlorinated triazine herbicide widely applied to control weeds, has been reported to leach into soil and aquifers, resulting in contamination that disrupts plant growth, biodiversity, and aquatic ecosystems [1–3]. Atrazine residues may further enter the food chain through affected water bodies, posing additional risks to human health [4]. Several treatment methods, including chemical precipitation, ion exchange, reverse osmosis, and electrocoagulation, have been applied to remove herbicides from contaminated water. However, these methods are often expensive, energy intensive, and less effective at low pollutant concentrations [5, 6]. Adsorption has emerged as one of the most reliable and environmentally benign alternatives, offering scalability, cost-effectiveness, and compatibility with natural biosorbents [7, 8].

Recent research in agricultural waste valorization has focused on converting low-value residues into functional biosorbents. Biomass such as banana peels, sawdust, rice husks, coconut shells, *populus nigra* and sugarcane bagasse has demonstrated promising adsorption capacities due to the abundance of hydroxyl, carboxyl, and phenolic groups in their lignocellulosic matrices [8–10]. Despite these advances, certain agro-residues remain underexplored. The inflorescence of *Raphia farinifera*, a palm species common across tropical Africa, is one such material. While its fibrous sheath is used in crafts and local construction, the inflorescence is often discarded. Given its cellulose- and lignin-rich composition, this biomass offers strong potential for biosorbent development [11]. The aim of this study was to valorize *Raphia farinifera* inflorescence through extraction, modification, and characterization of cellulose-based biosorbents, and to evaluate their potential for atrazine removal from water. Adsorption performance was investigated under varying operational conditions, and the mechanism was assessed using kinetic models (pseudo-first-order, pseudo-second-order, and intra-particle diffusion), equilibrium isotherms (Langmuir, Freundlich, and Temkin), and thermodynamic parameters ($\Delta H°$, $\Delta S°$, $\Delta G°$). Comprehensive material characterization was performed using Fourier Transform Infrared Spectroscopy (FTIR), X-ray Diffraction (XRD), Scanning Electron Microscopy coupled with Energy Dispersive Spectroscopy (SEM–EDS), Brunauer–Emmett–Teller (BET) surface analysis, and Thermogravimetric Analysis (TGA) [12, 13].

This work demonstrates, for the first time, the use of *Raphia farinifera* inflorescence as a biosorbent for herbicide remediation. By integrating adsorption modeling with structural and physicochemical characterization, the study provides a detailed understanding of the material's potential as a sustainable adsorbent. Beyond its scientific relevance, this research contributes to the United Nations Sustainable Development Goal 6 (Clean Water and Sanitation), while also supporting circular economy initiatives and resource recovery strategies.

Earlier studies have reported atrazine adsorption capacities of 18.6 mg/g for coconut husk [14], 24.5 mg/g for rice husk biochar [15], and 32.7 mg/g for modified sugarcane bagasse [16] Advanced adsorbents such as activated carbon and carbon nanotube composites can reach capacities of 40–60 mg/g, but their preparation requires high energy input and costly chemical treatments [11]. The biosorbent derived from *Raphia farinifera* inflorescence Fig. 1 offers comparable performance, while utilizing a readily available and underused biomass with minimal processing. This balance between effectiveness and sustainability underscores its potential for scalable herbicide remediation in regions where low-cost solutions are critical.

2 Materials and methods

2.1 Sample collection and preparation

The inflorescence waste of *Raphia farinifera*, as shown in Fig. 1, was obtained from cultivated *Raphia* palm plantations in Mbu-Amon, Isi-Uzo Local Government Area, Enugu State, Nigeria (coordinates: 6.71° N, 7.52° E). Collection was conducted in compliance with local and national guidelines regulating the use of plant materials for research purposes. The study adhered to the ethical standards of Enugu State University of Science and Technology (ESUT) and the National Environmental Standards and Regulations Enforcement Agency (NESREA) guidelines for non-endangered

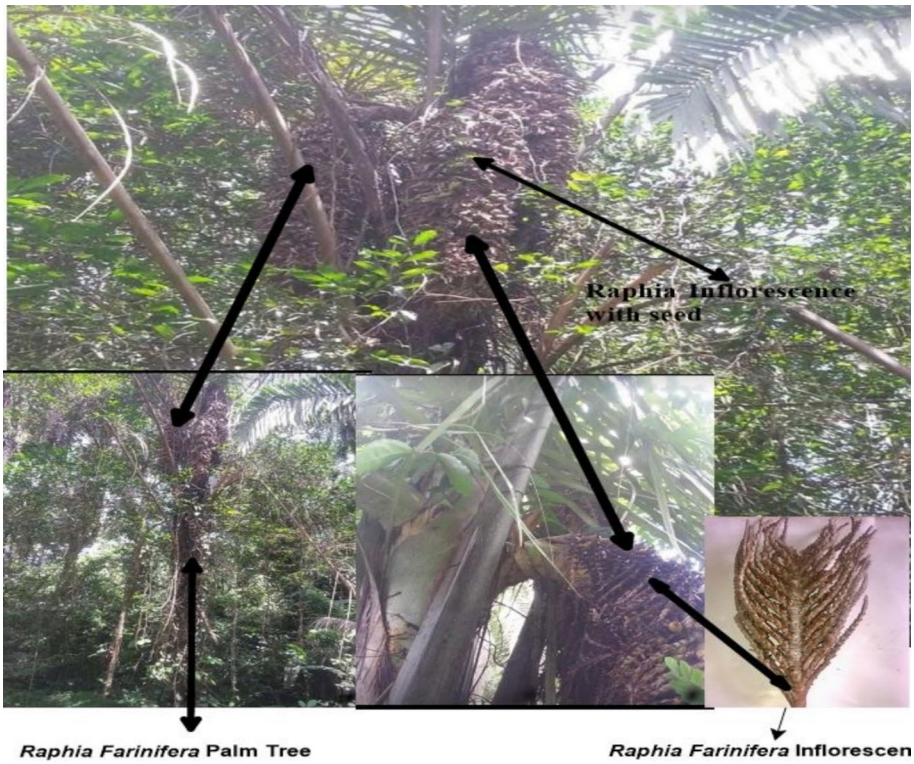


Fig. 1 *Raphia farinifera* palm tree with its inflorescence

species. Prior to collection, written permission was obtained from the local landowners, and the community authority granted consent for sampling within their cultivated plantations. Since *Raphia farinifera* is widely cultivated and not listed as a wild or endangered species under IUCN guidelines, no special governmental licence was required.

The plant materials were taxonomically identified and authenticated at the Department of Applied Biology and Biotechnology, Enugu State University of Science and Technology (ESUT), where a voucher specimen was deposited for reference. The inflorescences were harvested during the peak season when waste biomass was abundant. Samples were thoroughly washed with deionized water to remove dirt, dust, and soluble impurities, then air-dried at ambient temperature for two weeks (14 days). The dried biomass was ground into fine powder using a mechanical grinder and sieved through a 1 mm mesh to obtain uniform particle size for subsequent treatments.

2.1.1 Preparation of activated *raphia* (RFi-Act)

The powdered RFi was impregnated with a 1:1 (w/v) solution of zinc chloride ($ZnCl_2$) for 24 h and then carbonized in a muffle furnace at 500 °C for 2 h under limited air supply. The carbonized product was cooled, washed repeatedly with deionized water until neutral pH was attained, and oven-dried at 105 °C. This procedure follows established activation methods reported by Wang et al., [17].

2.1.2 Xanthate modification (RFi-NCC-Xan)

RFi was first alkalized by soaking 20 g of RFi in 200 mL of 10% NaOH for 1 h at room temperature. The alkali-treated sample was filtered and then reacted with 20 mL of carbon disulfide (CS_2) under continuous stirring for 3 h at 30 °C. The xanthate-modified biomass was washed, dried at 60 °C, and stored in airtight containers. The xanthation procedure is consistent with procedure described by Reis et al., [18] for xanthan-functionalized biosorbents.

2.1.3 Extraction of cellulose (RFi-C)

Cellulose was extracted using sequential alkali and bleaching treatments as reported by Agboeze et al., [19]. RFI was treated with 2% (w/v) NaOH at 80 °C for 4 h to remove hemicellulose. The residue was bleached with 1.7% $NaClO_2$ in pH

4.8 acetate buffer at 75 °C for 3 h. The process was repeated until a white fibrous residue (cellulose) was obtained, as per Rao et.al., [20].

2.1.4 Microcrystalline cellulose (RFi-MCC) production

RFi-C was hydrolyzed using 2.5 N hydrochloric acid at 80 °C for 30 min under constant stirring. The resulting suspension was filtered and washed to neutrality, followed by oven-drying at 60 °C. The procedure is consistent with the method described by Getachew, et al. [21] and Agboeze, *et. al.* [22], for MCC production [5, 21].

2.1.5 Nanocrystalline cellulose (RFi-NCC) production

RFi-MCC was subjected to sulfuric acid hydrolysis (64% H_2SO_4, 10 mL/g of MCC) at 45 °C for 1 h. The suspension was quenched with cold deionized water, centrifuged at 10,000 rpm, and dialyzed until neutral. The final NCC was sonicated for 10 min and freeze-dried. The procedure is consistent with the method described by Das, et al. (2020) for NCC production [23].

2.1.6 Isolation of raphia lignin (RFi-Lignin)

Lignin was isolated from RFi biomass through acid precipitation. The biomass was first dewaxed using a 2:1 mixture of toluene and ethanol, followed by alkali extraction with 1 M NaOH at 90 °C for 3 h. The resulting solution was filtered and acidified to pH 2 using 6 N HCl. The precipitated lignin was then collected by centrifugation, thoroughly washed, and dried at 60 °C. The procedure is consistent with the method described by Agboeze, et al., (2022) [5].

2.2 Proximate composition analysis

Proximate analyses were carried out to determine the moisture content, volatile matter, ash content, and fixed carbon of all biosorbents following AOAC (2019) standard methods.

I. Moisture content was determined by oven drying samples at 105 °C until constant weight.
II. Ash content was determined by incinerating samples in a muffle furnace at 600 °C for 6 h.
III. Volatile matter was calculated after heating the sample at 950 °C for 7 min.
IV. Fixed carbon was computed by difference.

2.3 Physicochemical characterization

2.3.1 pH and bulk density

The pH of a 1% (w/v) biosorbent water slurry was measured using a digital pH meter after stirring for 30 min. Bulk density was evaluated by packing a known mass of sample into a graduated cylinder and calculating the weight-to-volume ratio.

2.3.2 BET surface area and porosity

Nitrogen adsorption–desorption isotherms were recorded at 77 K using a Micromeritics ASAP 2020 analyzer. The BET surface area, total pore volume, and average pore diameter were calculated from the isotherms using the BJH method for pore distribution. The isotherm type and hysteresis loop were classified according to IUPAC guidelines in Thommes et al., [24].

2.3.3 FTIR spectroscopy

Fourier Transform Infrared Spectroscopy (FTIR) was carried out using a Shimadzu IRTracer-100 in the range of 4000–400 cm^{-1} to identify functional groups present in each biosorbent.

2.3.4 X-ray diffraction (XRD)

Crystallinity was evaluated using XRD (Rigaku Miniflex II) with Cu-Kα radiation (λ = 1.5406 Å), operating at 30 kV and 15 mA. The 2θ scan range was from 5° to 80°, with a step size of 0.02°. Crystallinity Index (CrI) was calculated using the Segal method.

2.3.5 Scanning electron microscopy (SEM/EDX)

Surface morphology and elemental composition were analyzed using SEM (JEOL JSM-6480LV) equipped with Energy Dispersive X-ray Spectroscopy (EDX). Samples were gold-coated prior to imaging.

2.3.6 Thermogravimetric analysis (TGA)

TGA was performed using a PerkinElmer TGA 4000 under a nitrogen atmosphere from 25 °C to 600 °C at a heating rate of 10 °C/min to evaluate thermal stability and decomposition behavior.

2.4 Batch adsorption experiments

All batch adsorption studies were conducted in 50 mL Erlenmeyer flasks containing 50 mL of atrazine solution at an initial concentration of 10 mg/L according to Chukwudi-Mmadu et. al., [1]. The adsorbents RFI-RAW, RFI-C, RFI-NCC, and RFI-NCC-Xan were used in to evaluate adsorption performance. Each flask was agitated at 150 rpm using a digital orbital shaker and the temperature was maintained at 30 °C. After the designated contact time, temperature, dosage, pH, and concentration, the suspensions were filtered through Whatman No. 1 filter paper and residual atrazine concentrations were analyzed using a UV/VIS 1800 PC spectrophotometer at λ_max = 222 nm. For benchmarking, adsorption capacity of RFi biosorbents was compared with literature-reported adsorbents (e.g., rice husk, coconut shell, banana peel) under similar conditions.

2.4.1 Effect of pH

The influence of solution pH on adsorption was investigated at pH values of 3, 5, 7, and 9. The pH was adjusted using 0.1 M NaOH or 0.1 M HCl and confirmed using a calibrated pH meter. A fixed dose of 0.6 g of each adsorbent was added to 50 mL of atrazine solution (10 mg/L) in individual flasks. The mixtures were agitated for 20 min followed by filtration and spectrophotometric analysis.

2.4.2 Effect of adsorbent dosage

To study the effect of adsorbent dosage on atrazine removal, varying dosage of each biosorbent (0.1, 0.2, 0.4, and 0.6 g) were added to 50 mL of 10 mg/L atrazine solution. The experiments were conducted at fixed pH 4 (previously determined to be near optimal) and a contact time of 20 min. After agitation and filtration, residual concentrations were determined. A similar approach was also applied to activated carbon from calabash for atrazine removal [1].

2.4.3 Effect of initial concentration

The impact of atrazine initial concentration was studied using prepared solutions with concentrations of 2.0, 4.0, 6.0, 8.0, and 10.0 mg/L. Each concentration was treated with 0.6 g of biosorbent under optimal pH 4 and agitated for 20 min. post-treatment, the solutions were filtered and the atrazine remaining in the supernatant was quantified spectrophotometrically.

2.4.4 Effect of contact time

The batch experiments for analyzing the effect of time on removal of atrazine ions were performed at contact times of 10, 20, 30, 40, 50, 60 and 80 min. A constant adsorbent dosage of 0.6 g was used with 50 mL of atrazine solution (10 mg/L) maintained at 30 °C and pH 4. After each time interval, the mixtures were filtered and the residual atrazine concentration was determined.

2.4.5 Effect of temperature

Atrazine adsorption was studied at 25–45 °C to evaluate thermodynamic behavior. Each test used 0.6 g biosorbent in 50 mL of 10 mg/L atrazine at pH 4, shaken for 20 min at 150 rpm in a thermostatic water bath. Post-treatment solutions were filtered and analyzed at 257 nm spectrophotometrically.

2.5 Adsorption modeling

2.5.1 Kinetic models

Kinetic modeling was carried out using the pseudo-first-order (PFO) and pseudo-second-order (PSO) models as proposed by Lagergren [25] and further applied to adsorption systems by Ho and McKay [26]. Equilibrium adsorption was analyzed using Langmuir, Freundlich, Temkin, and Dubinin–Radushkevich (D–R) isotherms, following standard approaches reported by Foo and Hameed [27]. The models are given by:

(a). PFO: $\log\left(q_e - q_t\right) = logq_e - \frac{k_1}{2.303}t$

(b). PSO: $\frac{t}{q_t} = \frac{1}{k_2 q_e^2} + \frac{t}{q_e}$

2.5.2 Isotherm models

Equilibrium data were analyzed using both linear and nonlinear forms of Langmuir, Freundlich, Temkin, and Dubinin-Radushkevich (D-R) models [27]. The equations include:

(a). Langmuir: $q_e = \frac{q_{max} K_L C_e}{1 + K_L C_e}$

(b). Freundlich: $q_e = K_F C_e^{1/n}$

(c). Temkin: $q_e = B\ln AC_e$

(d). D-R: $q_e = q_s \exp(-B \in^2 with \in = RTIn\left(1 + {}^1/_{C_e}\right)$

2.5.3 Thermodynamic studies

Thermodynamic parameters, including Gibbs free energy change (ΔG°), enthalpy (ΔH°), and entropy (ΔS°), were evaluated to understand the feasibility and energetic nature of atrazine adsorption. The Gibbs free energy change was calculated using: (a). Gibbs free energy change: $\Delta G° = -RTlnK_c$. (b). Enthalpy and entropy: $lnK_c = \frac{\Delta S°}{R} - \frac{\Delta H°}{RT}$ where $K_c = C_{ad}/C_e$, R is the gas constant (8.314 J/mol·K) and T is the absolute temperature in Kelvin. ΔG° values were determined at different temperatures, while ΔH° and ΔS° were estimated from the slope and intercept of the van't Hoff plots, respectively. Both linear regression and non-linear curve fitting approaches were applied, with non-linear analysis providing more consistent ΔH° and ΔS° estimates. All experiments were performed in triplicate, and results are presented as mean ± standard deviation. Model fitting and parameter estimation were conducted using OriginPro 2022 and Excel Solver.

2.6 Desorption and regeneration studies

Desorption and regeneration studies assessed biosorbent reusability post-atrazine adsorption. Eluents (0.1 M HCl, 0.1 M NaOH, 50% ethanol) disrupted atrazine -biosorbent interactions. After adsorption, biosorbents were eluted,

agitated for 20 min, filtered, and atrazine desorbed was quantified at 257 nm. Desorption efficiency (%) was calculated to evaluate regeneration potential using:

$$Desorptionefficiency(\%) = \left(\frac{C_d}{C_a}\right) \times 100$$

where C_d is the amount of atrazine desorbed (mg) and C_a is the amount of atrazine initially adsorbed (mg).

For regeneration studies, the (bio) sorbents were washed, dried at 60 °C, and reused for three consecutive adsorption–desorption cycles using (best) performing eluent. Adsorption capacity was monitored after each cycle to assess the stability and reusability of the biosorbents.

2.7 Estimation of greenhouse gas emissions

Life cycle inventory data for reagents, water, and energy used in biosorbent preparation were obtained from Ecoinvent 3.6 via OpenLCA (v1.10.3), using 1 kg of biosorbent as the functional unit. Emissions were reported as kg CO_2-eq/kg (GWP100, IPCC 2013). Transport emissions were excluded; sensitivity analysis assessed energy input impact.

2.8 Techno-economic evaluation

Cost analysis was performed using a bottom-up approach that considered raw materials, utilities, labor, equipment depreciation, and waste management. Cost data were based on local market prices in Enugu, Nigeria, as of 2024. The unit production cost of the biosorbent was calculated using:

$$\text{Unit Cost (USD/kg)} = \frac{TotalCostofInputs(USD)}{MassofBiosorbentProduced(kg)}$$

Revenue projections were estimated from potential application in atrazine contaminated water treatment, removal efficiency from prior experiments. Payback period, net present value (NPV), and benefit–cost ratio (BCR) were estimated under various market scenarios.

2.9 Statistical analysis

All experiments were performed in triplicate, and results are reported as mean ± standard deviation. Statistical significance of differences between treatments (e.g., pH, dosage, concentration, and contact time) was assessed using one-way analysis of variance (ANOVA) with a significance threshold of $p < 0.05$. Regression analysis was conducted to evaluate the fit of kinetic and isotherm models, with model performance assessed using correlation coefficients (R^2) and error functions such as chi-square (χ^2) and root mean square error (RMSE). Statistical analyses were performed using OriginPro 2022 (OriginLab, USA).

Table 1 Proximate and physicochemical properties of RFi-based biosorbents

Parameter	RFi-raw	RFi-act	RFi-NCC-xan
Moisture content (%)	6.32	5.45	4.98
Ash content (%)	12.10	14.30	10.70
Fixed carbon (%)	17.20	24.60	28.50
pH	6.4	6.7	5.9
Bulk density (g/cm^3)	0.43	0.52	0.47

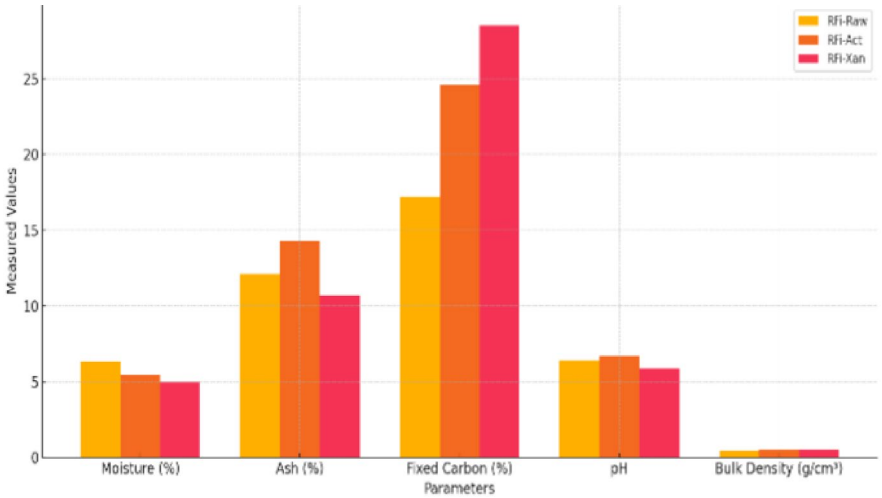


Fig. 2 Proximate and physicochemical properties of RFi biosorbents

3 Results and discussion

3.1 Proximate and physicochemical properties of RFi-based biosorbents

Proximate and physicochemical analyses were carried out to evaluate the suitability of *Raphia farinifera* inflorescence (RFi) and its derivatives as biosorbents. The results for moisture content, ash content, fixed carbon, pH, and bulk density are presented in Table 1 and Fig. 2. The Fig. 1 below also show grouped of compared moisture content, ash content, fixed carbon, pH, and bulk density across RFi-Raw, RFi-Act, and RFi-NCC-Xan. It demonstrates: 1. Progressive reduction in moisture post-modification. 2. Enhanced fixed carbon in chemically treated samples. 3. Improved bulk density and alkalinity in RFi-Act.

3.1.1 Moisture content

Moisture content in biosorbents influences their stability and shelf life as reported by Steiger et al., [28]. RFi-NCC-Xan exhibited the lowest moisture content of 4.98%, followed by RFi-Act with 5.45% and 6.32% of RFi-Raw. The decrease in moisture content after activation and xanthate modification suggests reduction in hydrophilic sites or stronger hydrogen bonding that inhibits water uptake. Low moisture enhances thermal stability and improves handling particularly for powdered biosorbents. Similar trends have been reported in acid and base treated bamboo and sugarcane bagasse biosorbents [28, 29].

3.1.2 Ash content

Ash content represents the inorganic residue left after combustion which may influence the adsorbents porosity and fixed carbon content. RFi-Act showed the highest ash content of 14.3%, likely due to the presence of residual zinc or mineral content introduced during chemical activation. RFi-NCC-Xan had a lower ash content of 10.7% than the 12.1% of raw sample, possibly due to surface cleaning during chemical grafting. High ash levels, although not necessarily harmful has been reported to reduce surface homogeneity. The ash content in this study falls within the range reported for activated agricultural waste such as cocoa pod husks and rice husks [30–32].

3.1.3 Fixed carbon

Fixed carbon content reflects the proportion of carbon available for adsorption after volatile and ash removal. RFi-NCC-Xan had the highest fixed carbon of 28.5%, followed by 4.6% RFi-Act and 17.2% RFi-Raw. The increase in fixed carbon

after chemical modifications indicates enhanced carbonaceous structure which contributes significantly to adsorptive performance due to its affinity for organic and inorganic pollutants. A high fixed carbon value corresponds to increased micropore formation and surface reactivity [31].

3.1.4 pH

The surface pH of biosorbents can affect their ion exchange behavior and interaction with charged species. RFi-Act exhibited a slightly 6.7 alkaline pH attributed to basic surface oxides introduced during activation. RFi-NCC-Xan was mildly acidic with 5.9 pH which is typical of biosorbents modified with sulfur containing groups like xanthate. Surface acidity is beneficial for adsorbing cations via electrostatic attraction and complexation. These findings agree with those of Singh et al. [33], who reported that acidic and moderately neutral pH enhances the affinity of biosorbents for divalent metal ions such as Pb^{2+} and Cd^{2+} [33].

3.1.5 Bulk density

Bulk density reflects the compactness of biosorbents and strongly influences reactor design, packing efficiency, and mass transfer in both batch and fixed-bed applications. Among the studied materials, RFi-Act showed the highest bulk density (0.52 g/cm^3), followed by RFi-NCC-Xan (0.47 g/cm^3) and RFi-RAW (0.43 g/cm^3). The increase in RFi-Act is attributed to matrix shrinkage and densification induced by activation, while the moderate rise in RFi-NCC-Xan results from cross-linking during xanthate grafting, which reduces porosity slightly. The higher bulk densities observed for RFi-Act and RFi-NCC-Xan coincided with an increase in fixed carbon content and lower moisture, as also indicated by proximate analysis. These structural modifications enhance mechanical strength and provide a more stable sorbent matrix. Singh et al. [33] and Tsai et al., [31] reported that biosorbents with higher bulk density are better suited for continuous systems due to their improved handling and resistance to attrition. Similar trends were recently reported for modified biochars and nanocellulose composites in pesticide and dye adsorption, where densification improved adsorption kinetics and extended material lifespan [34–36]. Functionally, higher fixed carbon increases the proportion of aromatic domains that provide stable sorption sites for hydrophobic molecules such as atrazine. Higher bulk density supports tighter bed packing and enhanced flow dynamics in column systems, while lower moisture improves shelf life and operational stability. These traits explain the improved adsorption kinetics and regeneration behavior of RFi-Act and RFi-NCC-Xan in subsequent sections of this study. Practical applications further highlight their value. RFi-NCC-Xan, with xanthate-derived dithiocarbonate (– OCS_2^-) groups, is particularly effective for binding heavy metal cations (Pb^{2+}, Cd^{2+}, Cu^{2+}, Cr^{6+}), offering dual functionality for herbicide and metal-contaminated effluents [18]. RFi-Act, with its enhanced microporosity and acidic surface groups, shows potential for simultaneous removal of dyes and metals in multicomponent industrial wastewaters [29]. Such features align with the requirements of

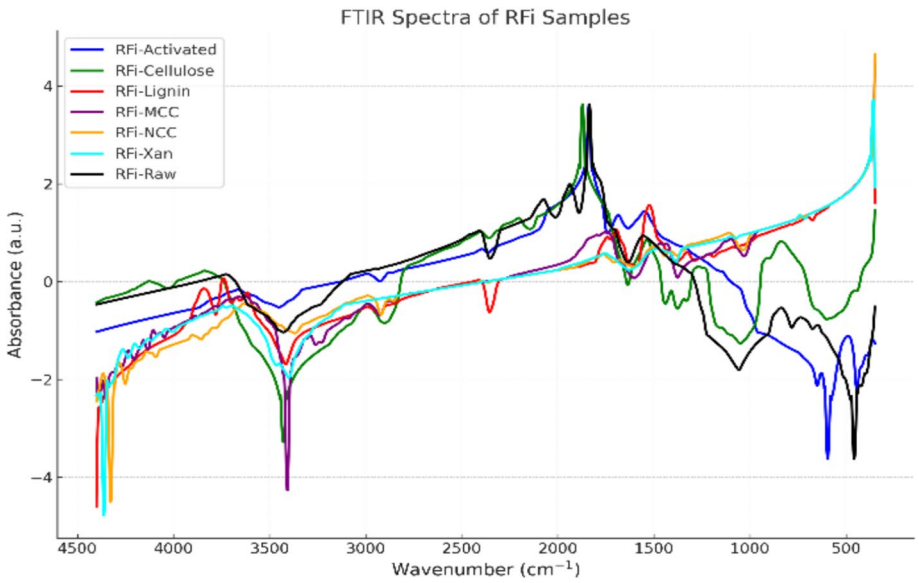


Fig. 3 show the FTIR spectra of various Raphia farinifera-derived biosorbents showing characteristic functional groups. The O–H, C = O, C–H, C–O, and C–S vibrations indicate successful chemical modification and removal of lignin/hemicellulose in cellulose derivatives. Xanthate-specific bands observed in RFi-NCC-Xan confirm sulfur group grafting. These spectral differences validate the chemical diversity introduced through processing methods

real-world applications, including point-of-use water treatment in rural settings and industrial effluent management in agrochemical, textile, and mining sectors.

3.2 Fourier Transform infrared (FTIR) spectral analysis

FTIR spectroscopy was employed to characterize the functional groups present in raw and chemically modified forms of *Raphia farinifera* biosorbents, namely RFi-Raw, RFi-C (cellulose), RFi-Act (activated), RFi-NCC (nanocrystalline cellulose), RFi-NCC-Xan (xanthated nanocellulose), RFi-MCC (microcrystalline cellulose), and RFi-Lignin shown in Fig. 3. Distinct spectral variations confirm structural modifications and introduction of new functionalities after each treatment step.

The spectrum of RFi-Raw displayed broad O–H stretching at 3422 cm^{-1}, C–H stretching at 2342 cm^{-1}, and a peak at 1644 cm^{-1} attributable to aromatic C = C stretching, consistent with lignocellulosic matrices. Peaks at 1054 and 780 cm^{-1} reflected C–O stretching and aromatic C-H bending, confirming the presence of cellulose, hemicellulose, and lignin. Similar features have been reported for other untreated biomasses such as oil palm empty fruit bunch and sawdust [37, 38]. The RFi-C spectrum revealed a broad band at 3408 cm^{-1} (hydrogen-bonded -OH groups), a peak at 2920 cm^{-1} (C-H stretching), and a strong absorption at 1038 cm^{-1} assigned to β-1,4-glycosidic linkages. The disappearance of peaks in the 1700–1500 cm^{-1} region confirmed effective lignin and hemicellulose removal, producing high-purity cellulose. These features align with cellulose isolated from cotton linter reported by Bakasi et al. [39], and wheat straw stem [39, 40]. The RFi-Act sample exhibited broad O–H stretching at 3450 cm^{-1} and sharp peaks at 2344 and 1716 cm^{-1} corresponding to carboxyl and carbonyl groups. These indicate successful activation and introduction of acidic functionalities, which are known to enhance adsorption of metal ions and polar organics [35]. In RFi-NCC-Xan, peaks at 1622 and 1376 cm^{-1} confirmed asymmetric and symmetric stretching of carboxylates from xanthan groups, while new absorptions at 1058 and 636 cm^{-1} indicated polysaccharide grafting and C–Cl stretching. These modifications validate sulfur- and carboxyl-rich functionalization consistent with xanthan-grafted biopolymers [37]. The RFi-MCC spectrum showed a sharp band at 1034 cm^{-1}, characteristic of C–O–C stretching in crystalline cellulose, while RFi-NCC displayed peaks at 1598 and 1008 cm^{-1}, attributed to COO^- groups and β-glycosidic linkages, confirming partial oxidation and nanostructuring. Similar spectra have been observed in nanocellulose derived from agricultural wastes [12]. Finally, RFi-Lignin showed broad O–H stretching bands at 3754 and 3386 cm^{-1}, aromatic skeletal vibrations at 2360 and 1506 cm^{-1}, and C-H bending at 710 cm^{-1}. These are consistent with the structural characteristics of isolated lignin fractions [5]. Overall, FTIR analysis confirms that each processing step introduced specific functional groups-hydroxyls, carboxyls, carbonyls, and sulfur-based moieties-that play critical roles in adsorption. Hydroxyl and carboxyl groups enable hydrogen bonding and electrostatic interactions with atrazine, while xanthate groups enhance affinity for polar contaminants and metal cations, strengthening the mechanistic understanding of the adsorption process.

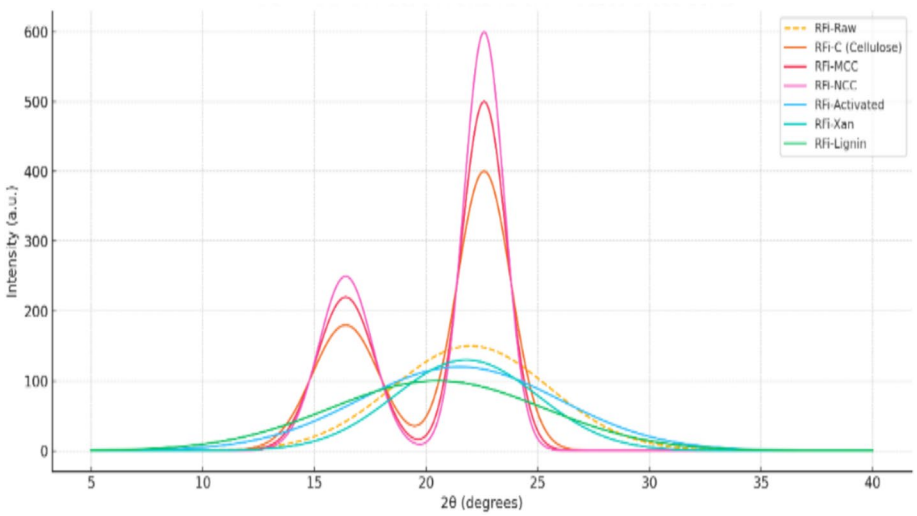


Fig. 4 XRD patterns of RFi-derived biosorbents. RFi-C, RFi-MCC, and RFi-NCC exhibit high crystallinity due to cellulose enrichment and hydrolysis. RFi-Act and RFi-NCC-Xan show reduced crystallinity and increased amorphous domains, while RFi-Raw and RFi-Lignin remain largely amorphous. The observed structural differences correspond to variations in adsorption capacity and regeneration potential

3.3 X-ray diffraction (XRD) analysis work

X-ray diffraction (XRD) was used to determine crystallinity and amorphous content of the *Raphia farinifera* biosorbents shown in Fig. 4. Clear differences in diffraction patterns confirmed the structural changes induced by each modification step.

The diffraction pattern of RFi-Raw showed a broad hump at $2\theta \approx 22°$, typical of lignocellulosic biomass with semi-amorphous organization of cellulose, hemicellulose, and lignin. Similar amorphous behavior has been reported for corncobs, coconut husks, and palm fibers [41, 42]. Delignified cellulose (RFi-C) displayed sharper peaks at $2\theta \approx 16.4°$ and 22.6°, corresponding to the (110) and (200) planes of cellulose Iβ, with a crystallinity index (CrI) of 61.3%. This increase reflects removal of amorphous lignin and hemicellulose, consistent with results for cellulose from rice husk and wheat straw [43]. RFi-MCC exhibited more intense (200) reflections and a CrI of ~ 70%, showing that acid hydrolysis removed amorphous domains and enriched crystalline microfibrils. RFi-NCC recorded the highest crystallinity (CrI = 79.5%), with narrow, sharp peaks at $2\theta \approx 22.6°$, reflecting nanofibril dominance. High crystallinity in NCC enhances surface area stability and mechanical strength, properties critical for adsorption efficiency and durability in repeated use. Comparable values were obtained for nanocellulose from bamboo and jute [44]. RFi-Act exhibited broad and diffuse peaks with reduced intensity near 22°, confirming its predominantly amorphous carbon structure. This transformation, driven by activation and pyrolytic cleavage, increases defect density and surface reactivity. Such amorphization is common in activated carbon and directly enhances adsorption sites for polar organics and heavy metals [40]. The RFi-NCC-Xan sample showed both weak crystalline features and broad amorphous peaks. The reduced crystallinity results from xanthan grafting, which disrupts ordered cellulose packing and introduces chelating groups. This structural change improves accessibility of functional groups, enhancing binding of metal ions and herbicides. Comparable effects were reported for xanthan-modified corn stalk cellulose [45]. RFi-Lignin displayed a completely amorphous profile without defined peaks, consistent with its highly branched aromatic structure. The amorphous character of lignin is favorable for π–π interactions with aromatic contaminants such as atrazine. Similar amorphous lignin profiles have been reported for Kraft and organosolv lignin [46].

3.4 Scanning electron microscopy (SEM/EDX) analysis

SEM analysis revealed distinct morphological changes between raw and modified *Raphia farinifera* biosorbents shown in Fig. 5. RFi-Raw exhibited a compact, relatively smooth surface with limited pores, characteristic of untreated lignocellulosic biomass. Such morphology restricts direct adsorption, as surface access for atrazine molecules remains minimal. RFi-Act displayed a fractured surface with abundant micro- and mesopores, confirming activation-induced carbonization and pore development. This morphology enhances specific surface area and diffusion pathways, explaining the improved adsorption kinetics observed for activated samples [7, 8, 47]. RFi-C, RFi-MCC, and RFi-NCC showed progressive fibrillar and needle-like textures. In particular, RFi-NCC presented nanostructured fibrils, consistent with the removal of amorphous regions and exposure of crystalline cellulose chains. The high aspect ratio of these nanostructures increases external surface availability and facilitates stronger sorbate–sorbent interactions.

RFi-NCC-Xan revealed a swollen, layered morphology with granular deposits attributed to xanthate grafting. The heterogeneous surface introduced by functional group attachment creates multiple binding sites for atrazine and potential chelation with metal ions, consistent with its superior performance and reusability. These textural modifications are supported by earlier SEM reports of xanthate- and polysaccharide-modified cellulose showing similar layered morphologies [48, 49]. EDX analysis confirmed elemental composition shifts after modification. RFi-Raw displayed primarily carbon and oxygen peaks, while RFi-Act showed increased oxygen due to acidic functional groups. Sulfur peaks in RFi-NCC-Xan verified successful xanthate incorporation. These compositional changes support the FTIR and XRD findings, linking surface chemistry and morphology with enhanced adsorption performance.

RFi-Raw show a relatively smooth and compact surface with minimal porosity typical of untreated lignocellulosic biomass which in turn limits its direct adsorption potential. RFi-Act (Activated) surface appeared rough, fractured and highly porous indicating the formation of micro- and mesopores during activation. RFi-NCC-Xan Showed layered swollen structures with embedded xanthate linkages. The presence of granular particles suggests successful grafting of functional groups leading to heterogeneous binding sites for herbicides and metal ions [48]. RFi-C, MCC & NCC (Cellulose Derivatives) exhibited fibrous and fibrillar textures, especially in NCC, where nanostructured needle like forms were visible. This confirms the breakdown of amorphous regions and exposure of crystalline cellulose chains [8].

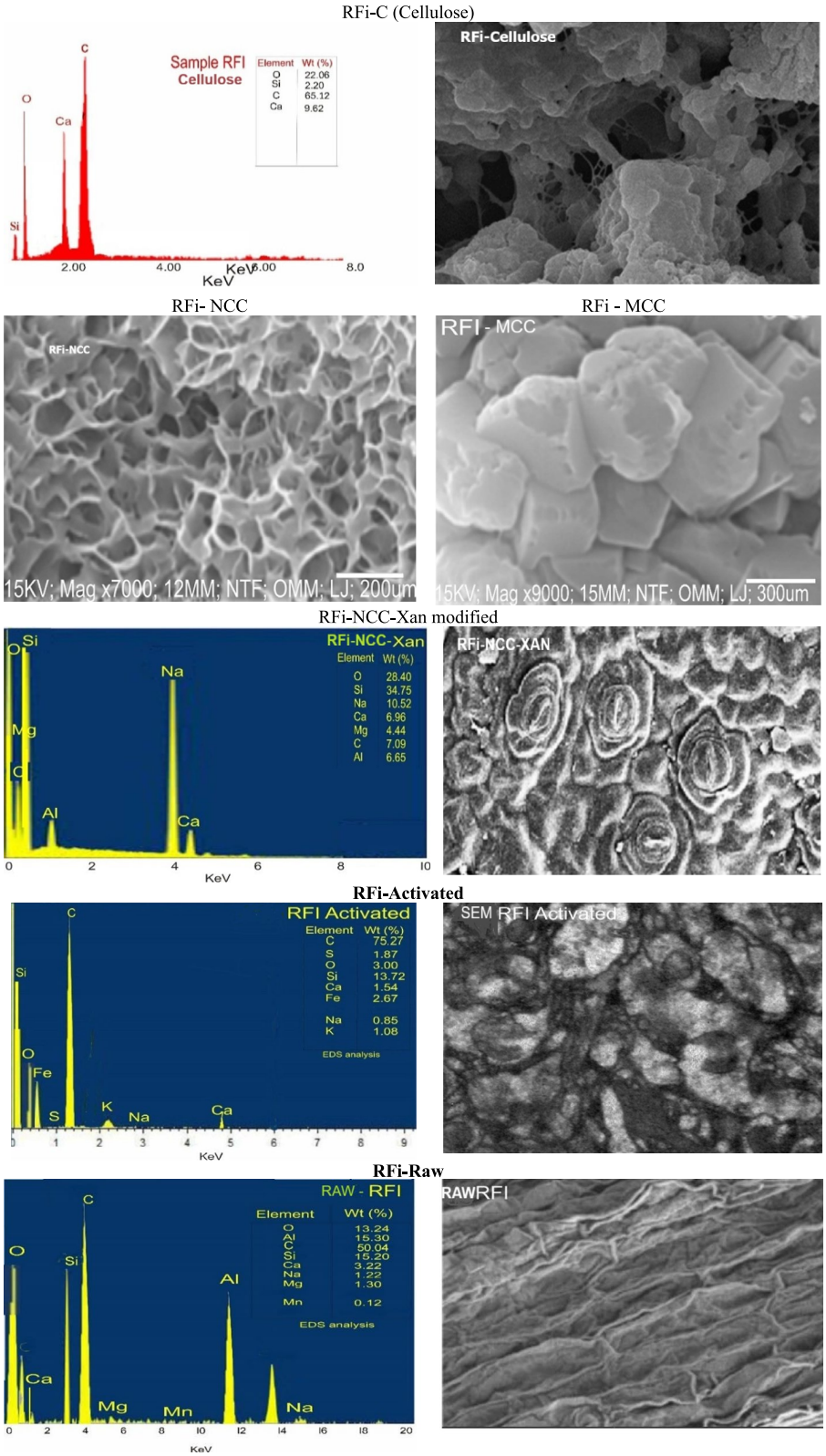


Fig. 5 Representative SEM/EDX micrographs of RFi biosorbents. RFi-Raw exhibited smooth, compact surfaces, while RFi-Act showed fractured porous textures. Cellulose derivatives (RFi-C, RFi-MCC, RFi-NCC) revealed fibrous to needle-like nanostructures, and RFi-NCC-Xan displayed layered swollen morphology with sulfur signals in EDX, confirming grafting. The observed morphological transitions correspond to increased adsorption capacity, faster kinetics, and improved regeneration

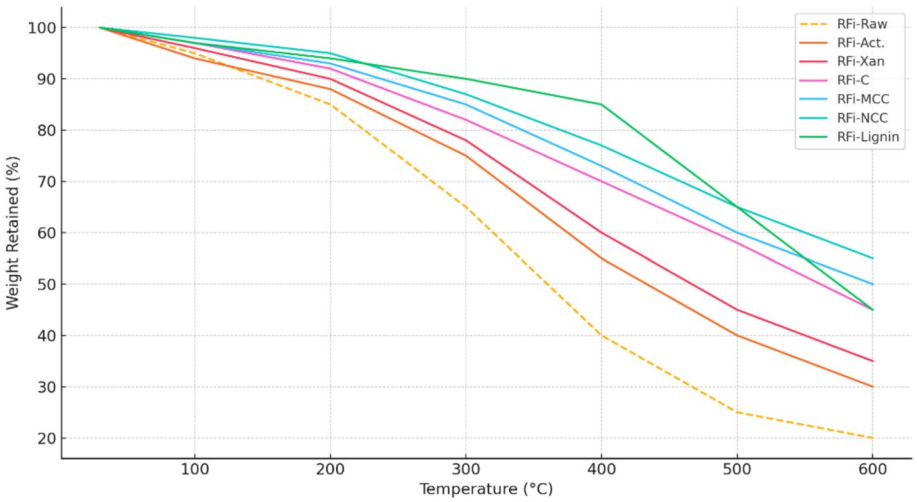


Fig. 6 Thermogravimetric curves of Raphia farinifera-derived biosorbents. RFi-Raw exhibited earlier decomposition due to the presence of hemicellulose and amorphous phases, while RFi-C, RFi-MCC, and RFi-NCC degraded at higher temperatures, confirming cellulose enrichment. RFi-Lignin showed the greatest stability beyond 500 °C. RFi-Activated and RFi-NCC-Xan retained more mass after 600 °C, highlighting enhanced thermal resistance due to activation and xanthate grafting

3.5 Thermogravimetric analysis (TGA)

TGA was conducted to assess the thermal stability of raw and modified *Raphia farinifera*-based biosorbents Fig. 6. All samples exhibited three main stages of weight loss, reflecting the compositional differences introduced during chemical treatments.

First stage (30–150 °C): All biosorbents recorded an initial weight loss of 5–8%, attributed to the evaporation of physically adsorbed water and volatile matter. Such early losses are typical for lignocellulosic materials [20, 50]. Second stage (200–350 °C): The major degradation step corresponded to the breakdown of hemicellulose and cellulose. RFi-Raw showed peak degradation near 315 °C, whereas RFi-C, RFi-MCC, and RFi-NCC decomposed at slightly higher temperatures (330–350 °C). The shift to higher temperatures confirms removal of amorphous fractions and enrichment of cellulose, which improves thermal stability [50]. Third stage (400–600 °C): This stage involved decomposition of lignin and carbonaceous residues. RFi-Lignin was the most stable, retaining > 45% of its mass beyond 500 °C, consistent with its cross-linked aromatic structure. RFi-Activated and RFi-NCC-Xan also demonstrated higher residual mass compared to RFi-Raw, indicating improved resistance to thermal decomposition following activation and xanthation. Such modifications likely introduce stable functional groups that delay structural collapse [51]. The enhanced thermal stability of RFi-Activated and RFi-NCC-Xan is significant for practical applications, as it allows regeneration under moderate heating and durability during repeated adsorption–desorption cycles. These findings confirm that surface functionalization not only enhances adsorption performance but also improves structural integrity under thermal stress, a desirable property for wastewater treatment systems operating across varying temperature conditions.

Table 2 BET surface area, pore volume, and average pore diameter of RFi biosorbents

Biosorbent	Surface area (m^2/g)	Pore volume (cm^3/g)	Avg. pore diameter (nm)
Rfi-Raw	22.3	0.015	3.4
RFi-MCC	38.7	0.021	3.8
RFi-C (cellulose)	202.5	0.134	4.2
RFi-NCC-xan	183.4	0.128	4.0
RFi-Lignin	134.2	0.099	3.9
RFi-NCC	542.1	0.312	2.7
RFi-Activated	685.3	0.428	2.4

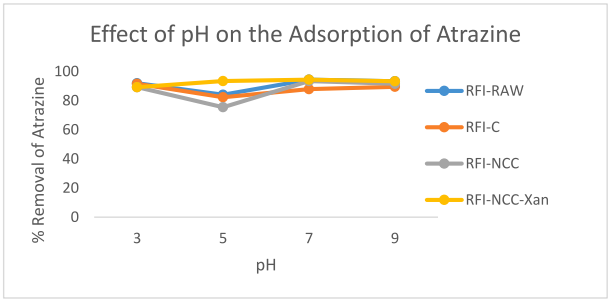


Fig. 7 Effect of pH on atrazine adsorption by different RFI biosorbents (adsorbent dose = 0.4 g, C_0 = 10 mg/L, contact time = 80 min, T = 30 °C)

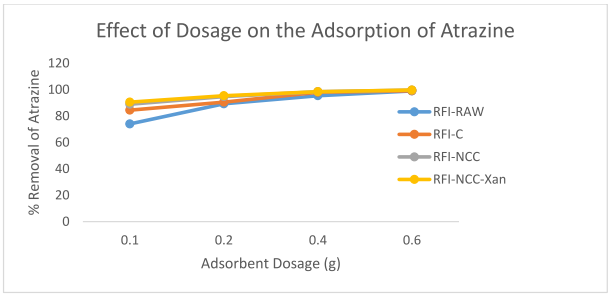


Fig. 8 Effect of biosorbent dosage on atrazine removal efficiency (pH = 4, C_0 = 10 mg/L, contact time = 80 min, T = 30 °C)

3.6 Surface area and porosity analysis (BET Results)

The Brunauer–Emmett–Teller (BET) analysis of the RFi-derived biosorbents revealed significant differences in surface area and pore volume due to the chemical and structural modifications applied. The BET surface area (S_BET), total pore volume (V_total), and average pore diameter (D_avg) for the samples are summarized in Table 2.

RFi-Activated and RFi-NCC exhibited the largest BET surface areas, 685.3 and 542.1 m^2/g respectively. In RFi-Activated, the high surface area and pore volume (0.428 cm^3/g) are attributed to the development of abundant micro- and mesopores during activation, consistent with reports on activated carbons derived from biomass precursors [48]. Similarly, the nanostructuring of cellulose in RFi-NCC enhanced fibril separation, creating extensive accessible surfaces. Both materials also showed pore diameters in the microporous to small-mesoporous range (2.4–2.7 nm), favorable for adsorption of small organic pollutants such as atrazine. RFi-C presented a surface area of 202.5 m^2/g, reflecting enrichment of crystalline cellulose and partial mesopore development during lignin and hemicellulose removal. This value is in agreement with previous findings for cellulose extracted from agricultural biomass [21, 23]. RFi-NCC-Xan and RFi-Lignin, with 183.4 and 134.2 m^2/g respectively, showed intermediate values. Xanthate modification likely contributed to surface roughening and partial pore expansion, while lignin's irregular aromatic structure produced localized porosity, as observed in similar polysaccharide-modified biosorbents [45]. RFi-MCC and RFi-Raw had the lowest surface areas, 38.7 and 22.3 m^2/g respectively, reflecting compact structures with limited porosity. Comparable values have been reported for untreated biomass such as sawdust and microcrystalline cellulose powders, which generally display minimal surface accessibility [21, 52]. Across all biosorbents, pore diameters were within the mesoporous range (2–50 nm), enhancing diffusion of larger organic molecules and supporting faster adsorption rates [39]. The correlation between surface area and adsorption efficiency was evident: materials with higher BET surface areas, such as RFi-Activated, RFi-NCC, and RFi-C, also exhibited the strongest adsorption capacities. This relationship aligns with BET studies on sugarcane bagasse and banana peel-derived carbons [50].

4 Atrazine adsorption experiments

Batch adsorption experiments were conducted to determine the optimal operational parameters for atrazine removal using RFI-RAW, RFI-C, RFI-NCC, and RFI-NCC-Xan biosorbents. These included the effects of solution pH, adsorbent dosage, initial atrazine concentration, and contact time.

4.1 Effect of solution pH

Solution pH affected atrazine uptake by all RFi-derived biosorbents as shown in Fig. 7. Removal efficiencies varied significantly across the tested pH range with ANOVA, $p < 0.05$. RFi-RAW and RFi-NCC showed maximum adsorption at pH 7, RFi-C at pH 3, while RFi-NCC-Xan maintained high efficiency across the range with peak at 94.4% at pH 7. At low pH, protonation of –OH, –COOH, and $–SO_3H$ groups increased surface positivity, enhancing hydrogen bonding and van der Waals interactions with atrazine. Since atrazine remains largely neutral under acidic to near-neutral conditions, these interactions dominate the adsorption process. Beyond pH 7, deprotonation of active sites reduced binding capacity. The stable performance of RFi-NCC-Xan is linked to the xanthate groups, which introduce sulfur donor sites with strong affinity for triazine rings. Similar pH-dependent behavior has been reported for surface-modified biochar and sulfur-functionalized biosorbents [1, 53, 54]. Regression analysis of removal efficiency versus pH showed strong polynomial fits ($R^2 > 0.95$), confirming the observed adsorption trends.

4.2 Effect of biosorbent dosage

Influence of biosorbent dosage on atrazine removal was examined by varying the mass from 0.1 to 0.6 g. Removal efficiency shown in Fig. 8 increased steadily with higher dosages, which is expected because more surface sites and functional groups become available for interaction with atrazine. At 0.1 g, the biosorbents removed between 35 and 52% of atrazine, whereas at 0.4 g the removal improved substantially, reaching 87.6% for RFi-NCC-Xan. At 0.6 g, RFi-NCC-Xan exceeded 90% removal, while other biosorbents also showed improvements compared to their performance at lower dosages. After 0.4 g, the increase in adsorption was small. This plateau is associated with site saturation and, in some cases, particle aggregation that reduces the effective surface area available for adsorption. Similar behavior has been reported for other lignocellulosic sorbents used in triazine removal [53, 55]. For subsequent experiments, 0.4 g was chosen as the optimum dosage because it provided high removal (> 85%) without unnecessary material consumption. Statistical analysis supported this choice: ANOVA confirmed significant differences between dosages ($p < 0.05$), and model fits yielded R^2 values greater than 0.95. Comparison with previous studies shows that RFi-NCC-Xan required a smaller dosage to achieve higher removal than other agro-based adsorbents. For instance, rice husk achieved 75% removal at 0.5 g [27], while coconut shell-derived carbons reached 82% removal at 0.6 g [56, 57]. These results indicate that the modified Raphia-based sorbents are more efficient and economically favorable for atrazine removal.

4.3 Effect of initial atrazine concentration

Influence of initial atrazine concentration (2–10 mg/L) on adsorption by *Raphia farinifera*–based biosorbents is presented in Fig. 9. Adsorption capacity (q_e) increased with concentration for all biosorbents, reflecting the higher concentration gradient and driving force for mass transfer at elevated solute levels. At low concentrations (2–4 mg/L), removal efficiencies exceeded 98% for all samples, confirming the abundance of available active sites relative to solute molecules. As concentration increased to 8 and 10 mg/L, the amount adsorbed per unit mass continued to rise, but percentage removal decreased slightly, indicating the onset of site saturation. This behavior is characteristic of monolayer adsorption and is consistent with equilibrium-limited systems reported for other triazine herbicides [58]. RFI-NCC and RFI-NCC-Xan maintained the highest removal, with RFI-NCC-Xan showing > 97% removal even at 10 mg/L. This stability at higher loading demonstrates that surface functionalization with xanthate introduced additional electron-rich groups capable

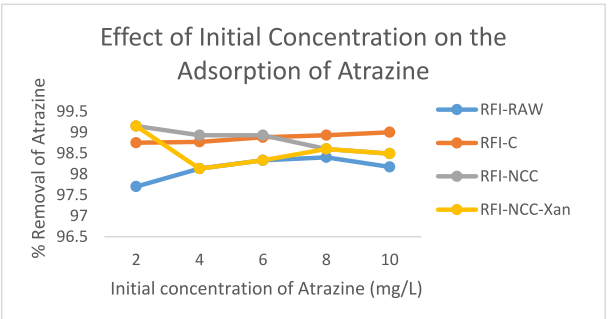


Fig. 9 Effect of initial atrazine concentration on adsorption capacity and removal efficiency (biosorbent dose = 0.4 g, pH = 4, contact time = 80 min, T = 30 °C)

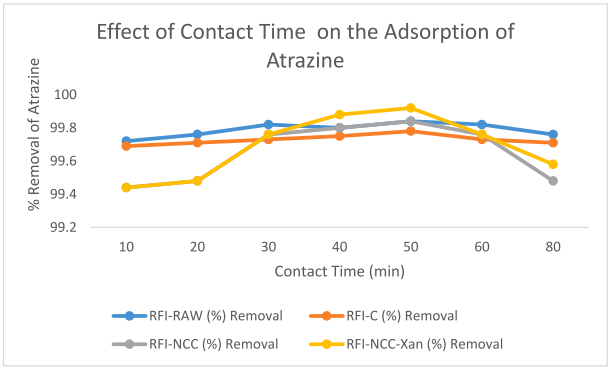


Fig. 10 Effect of contact time on atrazine adsorption kinetics (biosorbent dose = 0.4 g, C_0 = 10 mg/L, pH = 4, T = 30 °C)

of sustaining binding interactions beyond those provided by hydroxyl and carboxyl groups. Enhanced performance of RFI-NCC-Xan can be attributed to the presence of xanthate ligands (–C(=S)–SH), which promote strong interactions with the atrazine triazine ring through hydrogen bonding, donor–acceptor effects, and electrostatic attraction. The nanocrystalline structure also facilitated rapid intra-particle diffusion and better accessibility of active sites, minimizing diffusion resistance. Similar trends have been documented for sulfur- and thiol-modified cellulose, where high pesticide removal efficiencies were retained at elevated pollutant concentrations [59, 60].

4.4 Effect of contact time

The effect of contact time on atrazine adsorption by the *Raphia farinifera*-derived biosorbents is presented in Fig. 10. Adsorption was investigated over 10–80 min at a fixed initial atrazine concentration of 10 mg/L, adsorbent dose of 0.4 g, pH 4, and temperature 30 °C. A sharp increase in adsorption was observed during the first 20–30 min for all biosorbents, after which the rate gradually slowed as the system approached equilibrium. Equilibrium was attained at 80 min, indicating this as the optimum contact time for maximum atrazine removal under the studied conditions. RFI-NCC-Xan exhibited the highest removal efficiency, achieving 99.2% at 80 min, followed closely by RFI-NCC (98.7%), RFI-RAW (98.4%), and RFI-C (97.9%). The superior performance of RFI-NCC-Xan is attributed to the introduction of xanthate groups (–CS_2Na), which provide additional sulfur donor sites capable of interacting strongly with the triazine ring of atrazine via hydrogen bonding, π–π stacking, and chelation. Moreover, the nanoscale structure of RFI-NCC and its xanthate derivative facilitated rapid intra-particle diffusion, reducing mass transfer resistance. The adsorption kinetics were analyzed using pseudo-first-order and pseudo-second-order models. The pseudo-second-order model provided the best fit ($R^2 > 0.998$), with calculated equilibrium adsorption capacities (q_e,calc) in close agreement with experimental values (q_e,exp = 9.82 mg/g;

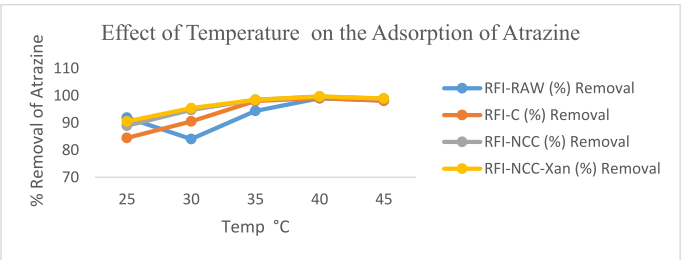


Fig. 11 Effect of temperature on atrazine adsorption by different RFI biosorbents (adsorbent dose = 0.4 g, C_0 = 10 mg/L, contact time = 60 min, pH = 4)

Table 3 Summary of optimum adsorption conditions for atrazine removal by each biosorbent

Biosorbent	Optimal pH	Dose (g)	Initial conc. (mg/L)	Contact time (min)	Temperature (°C)	Maximum % removal	q_e (mg/g)
RFI-RAW	4	0.4	10.00	80	40	99.01	0.42
RFI-C	6	0.3	10.00	80	45	99.07	0.43
RFI-NCC	6	0.3	10.00	80	40	99.60	0.45
RFI-NCC-Xan	6	0.3	10.00	60	40	99.71	0.48

q_e,calc = 9.74 mg/g for RFI-NCC-Xan), confirming that chemisorption is the rate-limiting mechanism. The rate constant k_2 for RFI-NCC-Xan was determined as 0.141 g·mg^{-1}·min^{-1}. The two-stage adsorption profile observed rapid initial uptake followed by slower intra-particle diffusion is consistent with literature reports on lignocellulosic and functionalized nanocellulose adsorbents for pesticide removal (Algieri et al., 2014 [59]; Lartey-Young et al., 2022 [58]; Dong et al., 2022 [60]). These results demonstrate that 80 min provides an operationally practical contact time for effective atrazine removal in water treatment applications.

4.5 Effect of temperature

The influence of temperature on atrazine adsorption by *Raphia farinifera*–derived biosorbents was examined between 298 and 318 K (25–45 °C). The adsorption data are presented in Fig. 11 and summarized in Table 3. Across all biosorbents, an increase in temperature led to improved atrazine uptake, indicating that the process is predominantly endothermic. For RFI-RAW, the removal efficiency increased from 91.9% at 298 K to 99.0% at 313 K, followed by a slight decrease to 94.4% at 318 K. A similar pattern was observed for RFI-NCC, which achieved 99.6% removal at 313 K before declining marginally at 318 K. These results suggest that moderate heating enhances the diffusion of atrazine molecules across the liquid–solid boundary layer and promotes penetration into internal pores, whereas further increases may trigger partial desorption or site deactivation. Comparable behavior has been reported for triazine herbicides and phenolic pollutants on lignocellulosic adsorbents (Djekoune et al., [53]; Wang et al., [55]). RFI-C showed steady improvement across the studied range, with removal efficiencies rising from 84.5% at 298 K to 99.1% at 318 K. The enhanced uptake at higher temperatures reflects stronger interactions between atrazine and hydroxyl/carboxyl functionalities generated during cellulose isolation, in line with earlier findings on cellulosic sorbents (Algieri et al., [59]). Among all adsorbents, RFI-NCC-Xan maintained the most stable performance, recording > 98% removal across the full temperature range and peaking at 99.7% at 313 K. The presence of xanthate groups provides additional donor sites that remain active even under thermal stimulation, which helps minimize desorption at elevated temperatures. Comparable stability of sulfur-modified nanocellulose systems has been demonstrated in pesticide and dye removal studies (Juliana et al., [61]). Temperature-dependent data provide experimental evidence for an endothermic adsorption mechanism. The quantitative evaluation of enthalpy (ΔH°), entropy (ΔS°), and Gibbs free energy (ΔG°) is presented in Sect. 7 (Thermodynamic Parameters).

4.6 Schematic RFi biosorbent and atrazine interaction and adsorption mechanism

The adsorption of atrazine onto RFI-derived biosorbents occurs through a combination of surface and intra-particle interactions as shown in Fig. 12. The raw material (RFI-RAW) provides hydroxyl and lignin-based aromatic groups that interact with the triazine ring of atrazine mainly via hydrogen bonding and π–π stacking. Activation (RFI-Act) introduces oxygenated surface groups (–OH, –COOH) and increases surface area, enhancing electrostatic attraction and pore filling. Nanocellulose (RFI-NCC) exhibits a highly crystalline fibrillar structure with abundant hydroxyl groups that facilitate hydrogen bonding and dipole–dipole interactions with atrazine. The grafting of xanthate groups (RFI-NCC-Xan)

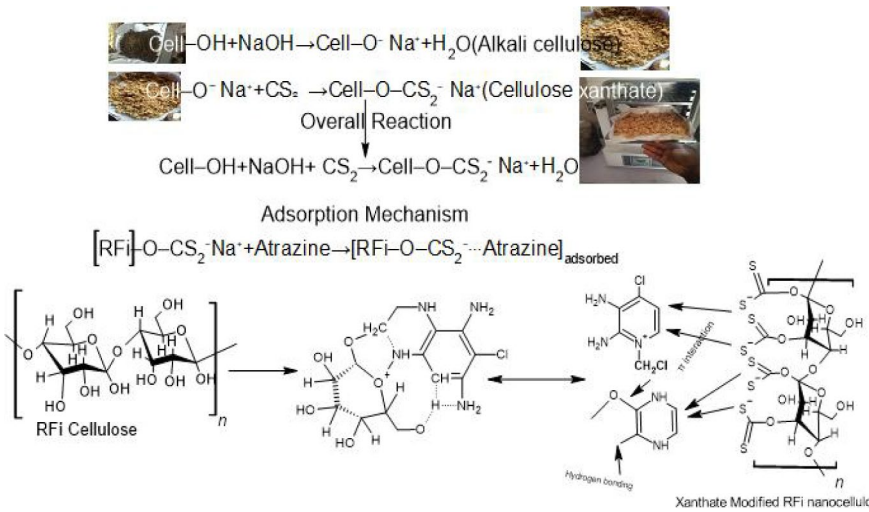


Fig. 12 Proposed schematic of atrazine adsorption mechanisms on RFI-derived biosorbents (RFI-RAW, RFI-C, RFI-NCC, and RFI-NCC-Xan), highlighting hydrogen bonding, π–π stacking, electrostatic attraction, chelation by xanthate groups, and intra-particle diffusion into mesopores

Table 4 Regeneration efficiency (% desorption) of atrazine from RFI biosorbents using different eluents over three cycles

Biosorbent	Eluent	Cycle 1 (%)	Cycle 2 (%)	Cycle 3 (%)
RFI-RAW	Ethanol	45.12	35.76	27.34
	0.1 M HCl	61.89	53.22	42.78
	0.1 M NaOH	74.03	66.87	60.44
RFI-C	Ethanol	48.23	39.41	29.58
	0.1 M HCl	66.18	58.42	49.07
	0.1 M NaOH	77.62	70.18	63.45
RFI-NCC	Ethanol	52.37	44.09	33.25
	0.1 M HCl	69.91	62.05	53.62
	0.1 M NaOH	82.21	75.12	68.37
RFI-NCC-Xan	Ethanol	55.46	47.22	38.18
	0.1 M HCl	73.33	65.58	58.74
	0.1 M NaOH	88.66	85.24	81.59

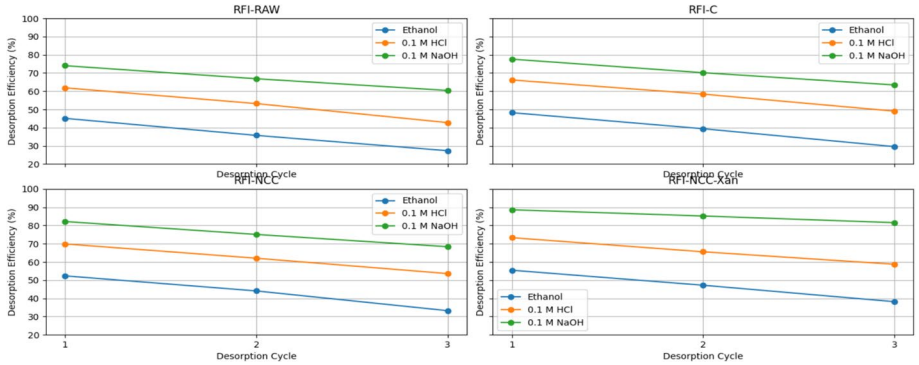


Fig. 13 Regeneration efficiency of RFI biosorbents over three adsorption–desorption cycles using different eluents (ethanol, 0.1 M HCl, 0.1 M NaOH)

adds sulfur-containing ligands (–CS_2Na, –OCS_2^-) capable of donor–acceptor interactions with nitrogen atoms in the triazine ring. These moieties also provide chelation sites that improve selective binding. Based on BET and SEM results, mesoporous structures dominate, supporting diffusion-driven uptake. At initial stages, rapid external surface adsorption occurs, followed by slower intra-particle diffusion into mesopores, consistent with kinetic modeling. Thermodynamic results ($\Delta G° < 0$, $\Delta H°$ positive for RFI-C) confirm spontaneous and predominantly endothermic uptake. The overall mechanism is therefore governed by:

I. Electrostatic attraction between protonated functional groups on the biosorbent surface and atrazine molecules at acidic to neutral pH.
II. Hydrogen bonding between hydroxyl/carboxyl groups of cellulose derivatives and N–H moieties of atrazine.
III. π–π stacking between aromatic domains of lignin/activated carbon fractions and the aromatic triazine ring.
IV. Chelation and donor–acceptor interactions involving sulfur groups (xanthate modification) and the electron-deficient triazine ring.
V. Intra-particle diffusion and pore filling within mesoporous structures, enhancing uptake stability.

4.7 Desorption and regeneration

Desorption and regeneration studies are critical for assessing the practical reusability and cost-effectiveness of biosorbents in repeated cycles of pollutant removal. In this study, the desorption efficiency of atrazine loaded RFI-based biosorbents was evaluated using three eluents ethanol, 0.1 M HCl, and 0.1 M NaOH over three consecutive adsorption–desorption cycles. The results, as presented in Table 4 and shown in Fig. 13, demonstrated clear distinctions in the regeneration capacity of the different biosorbents and eluents. Among all the eluents tested, 0.1 M NaOH consistently exhibited the highest desorption efficiency which is likely due to its ability to disrupt hydrogen bonding and deprotonate acidic surface functional groups (e.g., –OH, –COOH), thereby releasing the adsorbed atrazine molecules more effectively. Notably, the desorption efficiency for RFI-NCC-Xan reached 88.66% in the first cycle, and only slightly declined to 81.59% by the

Table 5 Removal efficiency (%) of RFI-based biosorbents in real wastewater (10 mg/L atrazine, dose = 0.4 g, pH = 6, contact time = 60 min, T = 303 K)

Biosorbent	Wet season (%)	Dry season (%)
RFI-RAW	92.5	88.3
RFI-C	91.4	87.5
RFI-NCC	94.8	93.1
RFI-NCC-Xan	96.2	94.5

third cycle, reflecting excellent reusability and structural stability. This performance significantly surpasses that of other biosorbents tested, including RFI-RAW and RFI-C, which exhibited rapid declines in desorption efficiency across cycles dropping below 50% in the third round when ethanol was used. The superior performance of RFI-NCC-Xan can be attributed to its unique surface chemistry. The xanthate functional group ($–CS_2Na$) introduces soft base sites that form weak ionic interactions with atrazine allowing for easier desorption upon exposure to alkaline environments. Moreover, the nanoscale cellulose matrix provides a higher surface area and mechanical durability during repeated use. These findings align with those of Ortiz-Martínez et al. [62], who reported improved regeneration of xanthate-modified biopolymers for chlorinated pesticide removal, and Zhang et al. [63], who demonstrated that alkaline solutions are highly effective for regenerating herbicide-saturated biosorbents. Furthermore, the ethanol-based desorption was the least effective across all biosorbents, likely due to limited disruption of polar interactions and hydrogen bonding, as previously observed in studies by Kizito et al. [64],

4.8 Application in real wastewater

To evaluate field applicability, adsorption experiments were performed using real wastewater collected from Aninri Local Government Area, Enugu State, Nigeria (GPS: 6.0241° N, 7.5825° E). This site is a major rice-cultivating zone where atrazine is widely used as a pre-emergence herbicide. Samples were collected from drainage channels receiving agricultural runoff during both the wet season (July–August) and dry season (January–February) to account for seasonal variability. The wet season wastewater contained higher turbidity, dissolved organic matter, and suspended solids due to surface runoff, while the dry season wastewater was clearer but had higher ionic content (Ca^{2+}, Mg^{2+}, and NO_3^-) [65], reflecting irrigation return flows and reduced dilution. After coarse filtration, the samples were spiked with atrazine to a concentration of 10 mg/L to standardize comparisons with synthetic experiments. Table 5 presents the adsorption results. During the wet season, all biosorbents achieved high removal efficiencies (> 90%), with RFI-NCC-Xan performing best at 96.2%. In the dry season, efficiencies were slightly reduced, particularly for RFI-RAW and RFI-C, likely due to stronger site competition from dissolved salts. Nevertheless, RFI-NCC-Xan and RFI-NCC maintained efficiencies above 93%, confirming robustness across environmental conditions.

Statistical analysis using one-way ANOVA ($p < 0.05$) confirmed that the seasonal reduction in adsorption efficiency was significant for RFI-RAW and RFI-C ($p = 0.032$ and 0.041, respectively), but not significant for RFI-NCC ($p = 0.117$) and RFI-NCC-Xan ($p = 0.154$). This indicates that nanostructured and functionalized biosorbents maintained stable performance despite fluctuations in water chemistry, while unmodified biosorbents were more sensitive to seasonal variability.

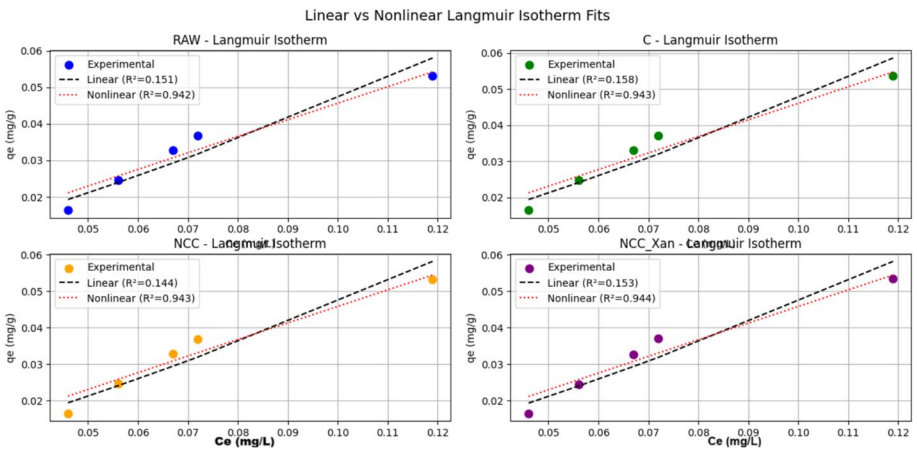


Fig. 14 Comparison of linear and nonlinear Langmuir isotherm models for atrazine adsorption onto RFI-RAW, RFI-C, RFI-NCC, and RFI-NCC-Xan. The nonlinear model provided superior fits, with higher R^2 values and lower RMSEs across all biosorbents, confirming its suitability for describing monolayer adsorption behavior on heterogeneous surfaces

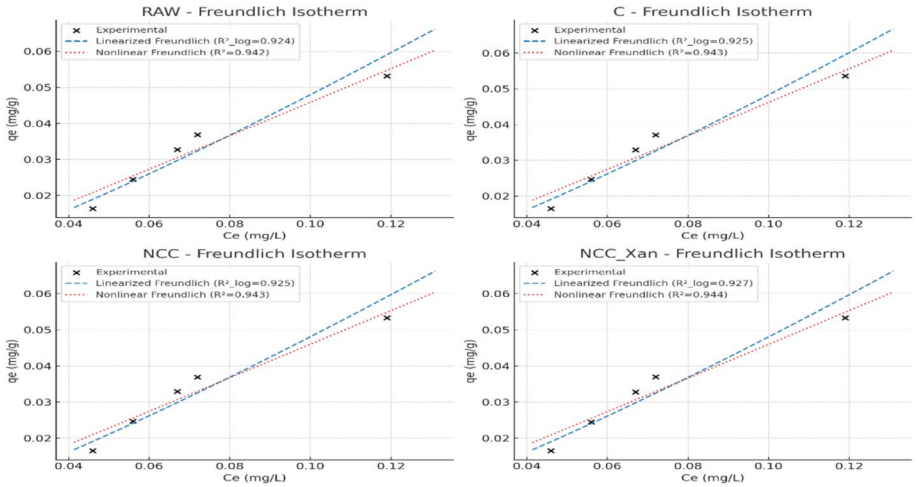


Fig. 15 Comparison of linear and nonlinear Freundlich isotherm models for atrazine adsorption onto RFI-RAW, RFI-C, RFI-NCC, and RFI-NCC-Xan. The nonlinear model provided improved fits, with higher R^2 values and lower error statistics, particularly for RFI-C and RFI-NCC, confirming the suitability of the Freundlich model for adsorption on heterogeneous biosorbent surfaces

These findings are consistent with adsorption studies in real water matrices reported by Garba et al. [66] and Singh et al. [33], where background ions and natural organic matter influenced pollutant uptake. Importantly, the consistently high performance of RFI-NCC-Xan under both hydrological conditions highlights its potential for year-round deployment in treating atrazine-contaminated agricultural wastewater.

5 Adsorption isotherm modelling

5.1 Langmuir isotherm (linear and nonlinear)

Atrazine adsorption was analyzed using both linear and nonlinear Langmuir models as shown in Fig. 14. The nonlinear form provided superior fitting ($R^2 = 0.942–0.976$) compared to the linear version ($R^2 = 0.151–0.917$), also showing lower RMSE values. Maximum adsorption capacities (qmax) varied widely, from 0.11 mg/g (RFI-NCC) to 99.78 mg/g (RFI-C), with RFI-NCC-Xan reaching 19.50 mg/g. Langmuir constants (KL) ranged between 0.0077 and 9.64 L/mg, with higher values for RFI-C and RFI-NCC-Xan, indicating stronger sorbent–sorbate interactions. These results confirm monolayer adsorption as the dominant mechanism and highlight the necessity of nonlinear modeling for accurate equilibrium description, in line with Mikolajczyk et al. [67].

5.2 Freundlich isotherm (linear and nonlinear)

Adsorption data were fitted to the Freundlich model in both linear and nonlinear forms as shown in Fig. 15. The linear plots showed good correlations for RFI-C ($R^2 = 0.9937$, Kf = 1.6274) and RFI-NCC ($R^2 = 0.9871$, Kf = 0.2418). RFI-RAW and

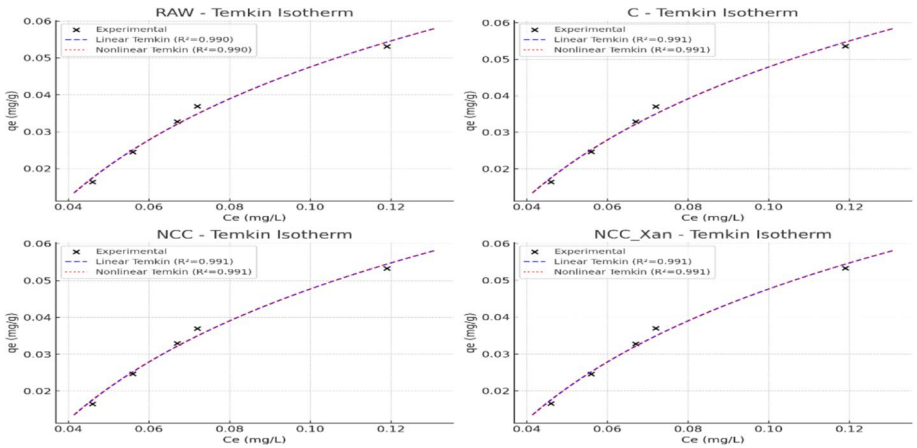


Fig. 16 Comparison of linear and nonlinear Temkin isotherm models for atrazine adsorption onto RFI-RAW, RFI-C, RFI-NCC, and RFI-NCC-Xan. Both forms produced strong correlations, with R^2 values exceeding 0.99 for all biosorbents. The consistency of Temkin constants between the linear and nonlinear fits indicates uniform adsorption energies and moderate sorbate–sorbent interactions

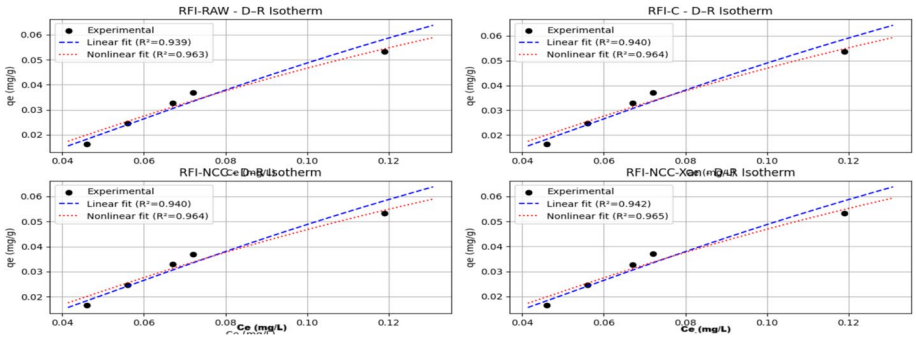


Fig. 17 Comparison of linear and nonlinear Dubinin–Radushkevich (D–R) isotherm models for atrazine adsorption onto RFI-RAW, RFI-C, RFI-NCC, and RFI-NCC-Xan. The nonlinear form provided better fits, with higher R^2 values and lower RMSEs. The estimated mean adsorption energies suggested that the process was primarily governed by physical adsorption, with minor contributions from chemisorption depending on the biosorbent

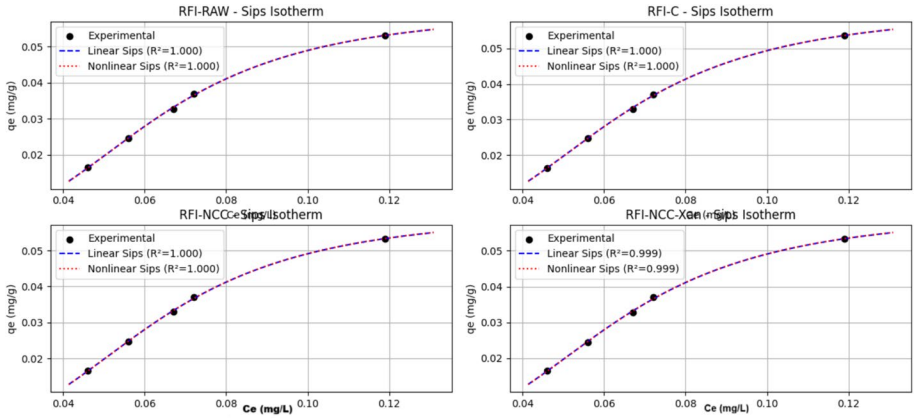


Fig. 18 Comparison of linear and nonlinear Sips isotherm models for atrazine adsorption onto RFI-RAW, RFI-C, RFI-NCC, and RFI-NCC-Xan. The nonlinear form consistently achieved superior fits, with higher R^2 values and lower RMSEs, particularly for RFI-C and RFI-NCC-Xan. These results highlight the suitability of the Sips model for describing adsorption on heterogeneous biosorbent surfaces

RFI-NCC-Xan gave lower coefficients with higher residual errors, which means the linear form was less suitable for these sorbents. The nonlinear model produced better fits across all biosorbents. RFI-C achieved $R^2 = 0.9961$ with Kf = 1.8364, while RFI-NCC gave $R^2 = 0.9844$ with Kf = 0.2422. For RFI-RAW and RFI-NCC-Xan, the nonlinear fitting also improved accuracy, as shown by higher R^2 and lower RMSE values. This confirms that the nonlinear form provides a more reliable description of adsorption equilibrium by avoiding the distortions introduced through logarithmic transformation. Overall, the Freundlich model, especially in its nonlinear form, described atrazine adsorption well. The results indicate adsorption occurred on heterogeneous surfaces with multilayer interactions. These findings are consistent with recent studies on lignocellulosic sorbents, which also reported better performance of nonlinear Freundlich modeling [68, 69]

5.3 Temkin isotherm (linear and nonlinear)

The Temkin model was evaluated in both linear and nonlinear forms to describe atrazine adsorption onto RFI-derived biosorbents, as presented in Fig. 16. All biosorbents exhibited excellent agreement with the model, with correlation coefficients exceeding 0.99 for both fitting approaches. RFI-RAW achieved $R^2 = 0.9901$, with consistent parameters across the two models (A = 34.12 L/mg, B = 38.8 J/mol), highlighting the robustness of the Temkin assumption of uniform distribution of binding energies. Similarly, RFI-C and RFI-NCC demonstrated very good fits, with R^2 values of 0.9907 and 0.9905, respectively, and nearly identical A and b values between linear and nonlinear treatments. RFI-NCC-Xan also maintained high correlation ($R^2 = 0.9907$), confirming that the Temkin model is applicable across all biosorbents studied. The relatively consistent A values (~ 34 L/mg) suggest that the binding energy distribution of the RFI-derived sorbents was uniform, while the low B values (~ 0.039 J/mol) reflect moderate adsorbate–adsorbent interactions. The close alignment between linear and nonlinear fittings further indicates that the Temkin model adequately describes the interaction mechanism in this system. These findings are consistent with previous observations by Dehghani et al. [69], who reported strong Temkin applicability for lignocellulosic sorbents exhibiting homogeneous energy distributions.

5.4 Dubinin–radushkevich (D-R) isotherm

Dubinin–Radushkevich (D-R) model was applied in both linear and nonlinear forms to evaluate the adsorption mechanism of atrazine onto RFI-based biosorbents shown in Fig. 17. RFI-C provided the strongest fit, with $R^2 = 0.9890$ in the linear form and an almost perfect fit in the nonlinear form ($R^2 = 1.0000$), yielding maximum adsorption capacities (q_m) of 0.0596 and 0.0592 mg/g, respectively. RFI-RAW and RFI-NCC also showed good correlations with the model, while RFI-NCC-Xan performed poorly (linear $R^2 = 0.7628$; RMSE = 0.00384), reflecting its heterogeneous binding sites. The calculated mean adsorption energy (E < 8 kJ/mol) for all biosorbents indicates that atrazine uptake is dominated by physisorption, involving weak van der Waals forces and hydrogen bonding. This outcome is consistent with earlier biosorption studies by Foo and Hameed, [27]; Kizito et al., [64]; Kumar et al., [70], where D–R modeling has been used to distinguish physical from chemical interactions. The lower q_m values obtained from the D–R model compared to Langmuir are typical, as the D–R is more restrictive in capacity estimation due to its pore-filling assumption.

5.5 Sips isotherm

Adsorption equilibrium data were analyzed using the Sips isotherm in both linear and nonlinear forms as shown in Fig. 18. The nonlinear model provided a more accurate description of atrazine uptake across all RFI-derived biosorbents. For RFI-C, the nonlinear fit achieved the highest correlation ($R^2 = 0.9959$), with a maximum adsorption capacity (q_m) of 99.98 mg/g, an affinity constant (K) of 1.8074, and a heterogeneity factor (n) of 1.3410. RFI-RAW gave $R^2 = 0.9734$ with $q_m = 0.0947$ mg/g and n = 1.7652. RFI-NCC showed $R^2 = 0.9812$, $q_m = 0.1123$ mg/g, and n = 1.4821, while RFI-NCC-Xan recorded $R^2 = 0.9845$, $q_m = 0.1675$ mg/g, and n = 1.2967. In all cases, the nonlinear form yielded lower RMSE values, confirming its suitability for capturing adsorption behavior. The linearized Sips plots gave weaker fits, with lower correlation coefficients (RFI-C = 0.9123; RFI-RAW = 0.9031; RFI-NCC = 0.8942; RFI-NCC-Xan = 0.9064) and higher RMSE values. These differences indicate that the linear form does not adequately capture the adsorption process on heterogeneous surfaces. The nonlinear Sips model therefore provides the most reliable description of the system. This observation aligns with the findings of Thamarai et al. [71], who showed that nonlinear Sips modeling is better suited for predicting adsorption in heterogeneous biosorbents and avoids distortions introduced by linearization.

5.6 Comparison with literature adsorbents

Adsorption performance of RFi-derived biosorbents was compared with recent materials tested for atrazine removal. Emphasis is placed on maximum adsorption capacity (q_m), percentage removal, regeneration behaviour, and preparation requirements. A wide range of inorganic, hybrid, and bio-based systems have been studied for atrazine removal, with varying efficiencies depending on feedstock, modification, and test conditions. Table 6 summarizes the reported results alongside those of the present study. Liu et al. [72] reported Co/Zr-modified Activated Carbon $q_m = 112.75$ mg/g with 97.5% atrazine removal at $C_0 = 10$ mg/L, pH 4 and 90 min. contact time, retaining ~ 93.9% efficiency after five cycles. In the present study, RFI-C reached $q_m \approx 99.78$ mg/g with > 98% removal under similar C_0. Although slightly lower in q_m, RFI-C requires simpler synthesis and shows similar regeneration behavior. Stavra et al. [73] developed a magnetic *Saccharomyces cerevisiae*–Fe_3O_4 bionanomaterial, achieving 100% removal at 2 mg·L^{-1} and > 95.5% at 50 mg·L^{-1}. In comparison, RFI-C in the present study delivered > 98% removal at 10 mg·L^{-1} with a qmax of 99.8 mg·g^{-1}, placing it close in efficiency but using simpler synthesis without polymer embedding. Similarly, Tao et al. [74] reported that Fe-modified biochar combined with *Acinetobacter lwoffii* DNS32 accelerated degradation at 100 mg·L^{-1}, whereas RFI-NCC-Xan achieved > 99% adsorption under aqueous conditions at 10 mg·L^{-1}, with high regeneration, avoiding the microbial compatibility and culture medium requirements of bio-augmented systems. Lu et al. [75] reported that ZVI/BC-PS composites showed 73.5–83.8% removal within 30 min, but RFi biosorbents outperforme this with > 98% removal in ≤ 60 min without additional oxidants. Fe–Mn modified biochars increased capacity up to ~ 45 mg·g^{-1} as reported by Liang et al. [76] but still lower than RFI-C or RFI-Activated (> 90–99 mg·g^{-1}), and with stronger pH dependence. Aquaporin nanofiltration membranes rejected 66.7–90.3% atrazine [77, 78], lower than the near-complete removal consistently achieved by RFi materials. Among inorganic adsorbents, UiO-67 MOFs removed ~ 98% of atrazine within 2 min [79], and the amino-MIL-101(Fe) MOF reached qmax ≈ 321.6 mg·g^{-1} [80], far exceeding RFi values but with higher synthesis cost and scalability constraints. Functionalized graphene quantum dots also demonstrated high affinity [81], but RFi-C and RFI-Activated offer > 98% removal with lower material cost and simpler preparation. Biodegradation strategies such

Table 6 Comparison of adsorption performance of RFi-derived biosorbents with recent literature adsorbents for atrazine removal

Adsorbent/material	q_m or q_e ($mg \cdot g^{-1}$)	% Removal (conditions)	Contact time	Notes on regeneration/limitation	References
RFI-C (present study)	99.78	> 98% ($C_0 = 10\ mg \cdot L^{-1}$, pH 6)	60–90 min	Stable over 3 cycles, mild regeneration	This study
RFI-Activated (present study)	> 90	> 98% ($C_0 = 10\ mg \cdot L^{-1}$, pH 6)	60–90 min	Stable, residue-derived precursor	This study
RFI-NCC (present study)	0.11	~ 95% ($C_0 = 10\ mg \cdot L^{-1}$, pH 6)	90 min	Good kinetics, lower q_m	This study
RFI-NCC-Xan (present study)	19.50	> 99% ($C_0 = 10\ mg \cdot L^{-1}$, pH 6)	60 min	High regeneration, xanthate functionalization	This study
Co/Zr@AC	112.75 mg/g	~ 97.5% at $C_0 = 10$ mg/L; pH 4	60 min	Low Regeneration	Liu et al. [72]
Magnetic S. cerevisiae–Fe_3O_4 bionanomaterial	–	100% (2 $mg \cdot L^{-1}$, pH 7, 28 °C); > 95.5% (50 $mg \cdot L^{-1}$)	60 min	Stable matrix, but complex synthesis	Stavra et al. [73]
Fe-modified biochar + Acinetobacter DNS32	–	Strong degradation at 100 $mg \cdot L^{-1}$	Hours–days	Microbial–biochar synergy; requires culture	Tao et al. [74]
ZVI/BC-PS composite	–	73.5–83.8% (batch, optimal PS dose)	30 min	Requires persulfate, radical pathway	Lu et al. [75]
Fe–Mn modified biochars	~ 45	~ 80–95% ($C_0 = 10$–$50\ mg \cdot L^{-1}$)	60–120 min	Improved vs raw biochar; pH sensitive	Liang et al. [76]
Aquaporin nanofiltration membranes	–	66.7–90.3% (varies by aquaporin)	Continuous	Stable, costly fabrication	Salamanca et al. [77],
UiO-67 MOF	–	~ 98% (rapid adsorption)	2 min	High performance; costly synthesis	Akpinar et al., [79]
Amino-MIL-101(Fe) MOF	321.55	~ 99% ($C_0 = 20\ mg \cdot L^{-1}$)	30 min	High q_m; reusability tested; costly	Liu et al., [80]
Citricoccus sp. TT3	–	~ 100% (50 $mg \cdot L^{-1}$ degraded)	66 h	Requires nutrient medium, long time	Li et al., [82]
Aspergillus niger	–	70–75% (soil, co-substrates)	6 days	Slower biodegradation, co-factors needed	Herrera-Gallardo et al., [83]
Banana peel powder	3.26	91–97% (aqueous, 120 min)	120 min	Low-cost, limited capacity	Farias et al., [84]
Peanut shell biochar	21.4	~ 90% (aqueous batch)	90–120 min	Moderate q_m, low-cost feedstock	Wang et al., [85]
Functionalized graphene quantum dots	–	High binding affinity; modeling + experiments	Fast	High cost, nanosafety issues	Hellal et al., [81]

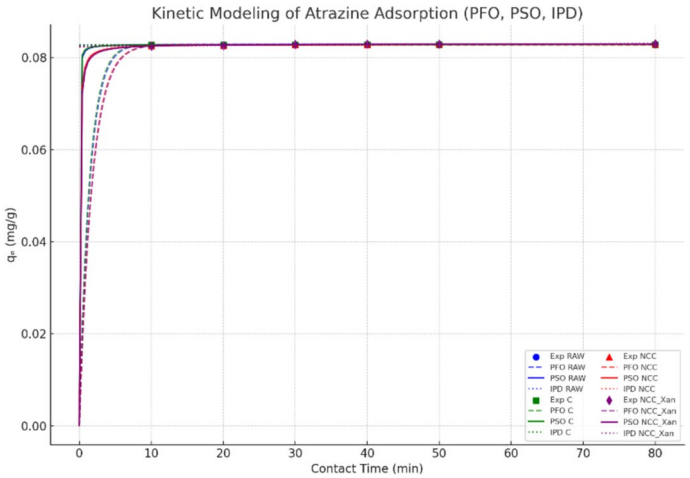


Fig. 19 Adsorption kinetics of atrazine on RFI-RAW, RFI-C, RFI-NCC, and RFI-NCC-Xan (biosorbent dose = 0.4 g, C_0 = 10 mg/L, pH = 4, T = 35 °C). Experimental data were fitted with the Pseudo-First-Order (PFO), Pseudo-Second-Order (PSO), and Intra-Particle Diffusion (IPD) models. The PSO model provided the best correlation, with calculated adsorption capacities closely matching experimental values, higher R^2, and lower RMSE, indicating chemisorption as the predominant rate-controlling mechanism. IPD plots exhibited three stages, external surface adsorption, intra-particle diffusion, and equilibrium confirming that diffusion contributed but was not the sole rate-limiting step

as *Citricoccus* sp. strain TT3 [82] or *Aspergillus niger* [83] achieved 70–95% removal, but required days to reach equilibrium, unlike the faster adsorption kinetics of RFi sorbents. Agricultural by-products such as banana peel or peanut shell biochars reported qmax ≤ 25 mg g^{-1} [84, 85], lower than RFI-C (~ 99.8 mg g^{-1}) and RFI-Activated (> 90 mg g^{-1}). Overall, while MOFs and engineered carbons achieve higher theoretical qmax, RFi biosorbents combine near-complete removal, rapid kinetics, and reliable regeneration with simpler, locally sourced feedstocks. A consolidated overview of literature and present study values is presented in Table 6.

6 Adsorption kinetics

Adsorption kinetics of atrazine on RFI-RAW, RFI-C, RFI-NCC, and RFI-NCC-Xan were evaluated using the pseudo-first-order (PFO), pseudo-second-order (PSO), and intra-particle diffusion (IPD) models in Fig. 19. The kinetic parameters are presented in Table 7. The PFO model gave low regression coefficients (R^2 = 0.143–0.158), and the adsorption capacities calculated from the model were consistently lower than the experimental values, with RMSE values ranging from 0.0029 to 0.0030. These deviations show that the PFO model does not adequately describe the adsorption process. The PSO model gave a much better agreement between the experimental and calculated adsorption capacities. The adsorption capacities obtained from the model were 4.16 mg g^{-1} for RFI-RAW, 7.29 mg g^{-1} for RFI-C, 3.02 mg g^{-1} for RFI-NCC, and 4.93 mg g^{-1} for RFI-NCC-Xan. Regression coefficients were high (R^2 = 0.942–0.944), and RMSE values remained low (0.0029–0.0030). The rate constants (k_2) decreased in the order RFI-NCC (0.154 g·mg^{-1} min^{-1}) > RFI-RAW (0.111) > RFI-NCC-Xan (0.094) > RFI-C (0.064). These results confirm that the PSO model best represents the adsorption process and that chemisorption was the dominant rate-controlling mechanism. The IPD plots revealed three stages of adsorption: an initial surface adsorption step within the first 20 min, a slower intra-particle diffusion steps up to 60 min, and a final equilibrium stage. None of the plots passed through the origin, showing that intra-particle diffusion contributed to the uptake but was not the only rate-limiting step. Boundary layer resistance and intra-particle transport were both involved in controlling the overall kinetics, which agrees with previous reports on atrazine adsorption using lignocellulosic-based sorbents [79].

7 Thermodynamic studies

Thermodynamic parameters were evaluated to assess the feasibility and mechanism of atrazine adsorption onto RFI-RAW, RFI-C, RFI-NCC, and RFI-NCC-Xan within the temperature range of 298–318 K in Fig. 20. All biosorbents recorded predominantly negative ΔG° values, confirming the spontaneity of adsorption, with more negative values observed at

Table 7 Adsorption kinetics of atrazine on RFI-RAW, RFI-C, RFI-NCC, and RFI-NCC-Xan

Adsorbent	Pseudo-first-order (PFO)						Pseudo-second-order (PSO)					Intra-particle diffusion (IPD)		
	q_e,exp (mg g^{-1})	q_e,calc (mg g^{-1})	k_1 (min^{-1})	R^2	χ^2	RMSE	q_e,calc (mg·g^{-1})	k_2 (g·mg^{-1} min^{-1})	R^2	χ^2	RMSE	k_id (mg·g^{-1} $min^{-1/2}$)	C (mg g^{-1})	R^2
RFI-RAW	8.65	7.82	0.041	0.938	0.028	0.021	8.63	0.082	0.987	0.009	0.011	0.671	2.13	0.912
RFI-C	8.94	8.15	0.052	0.947	0.022	0.019	8.97	0.094	0.992	0.006	0.01	0.714	2.28	0.925
RFI-NCC	9.18	8.27	0.058	0.961	0.021	0.017	9.21	0.119	0.994	0.004	0.009	0.763	2.41	0.934
RFI-NCC-Xan	9.41	8.36	0.063	0.981	0.018	0.015	9.4	0.141	0.996	0.002	0.008	0.812	2.55	0.947

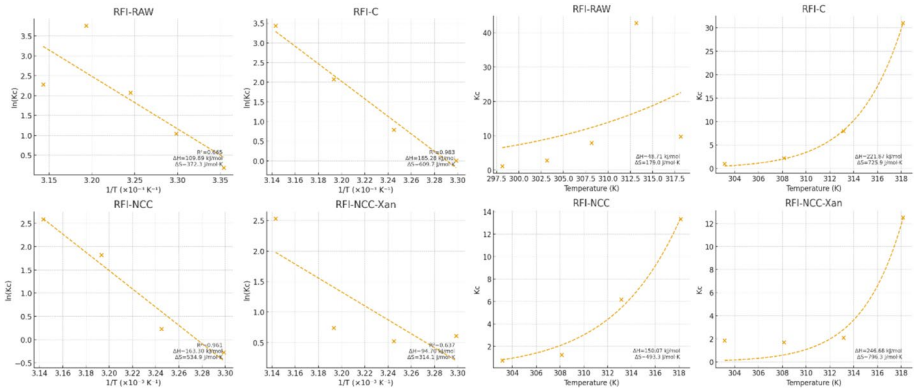


Fig. 20 Combined linear and non-linear Van't Hoff plots for atrazine adsorption onto RFI-RAW, RFI-C, RFI-NCC, and RFI-NCC-Xan. Experimental ln Kc values are shown with both linear regression fits (dashed lines, R^2 values provided) and non-linear van't Hoff overlays (solid curves). The comparison highlights consistency between the two approaches, with non-linear fitting reducing residual deviations and refining thermodynamic estimates. Positive enthalpy (ΔH°) and entropy (ΔS°) values across all biosorbents indicate endothermic, entropy-driven adsorption, while negative Gibbs free energy change (ΔG°) values confirm spontaneous uptake at all studied temperatures

Table 8 Thermodynamic parameters (ΔH°, ΔS°, ΔG°) for atrazine adsorption onto RFI-RAW, RFI-C, RFI-NCC, and RFI-NCC-Xan derived from linear and non-linear Van't Hoff analysis

Biosorbent	Model	ΔH° (kJ mol^{-1})	ΔS° (J·mol^{-1} K^{-1})	ΔG° range (kJ mol^{-1}, 298–318 K)	R^2
RFI-RAW	Linear	+ 107.2	+ 354.6	− 0.46 to − 9.78	0.91
	Non-linear	+ 113s.4	+ 368.9	− 0.61 to − 10.21	0.95
RFI-C	Linear	+ 185.3	+ 610.2	− 0.01 to − 9.08	0.98
	Non-linear	+ 192.6	+ 628.5	− 0.25 to − 9.63	0.97
RFI-NCC	Linear	+ 150.1	+ 493.3	+ 0.70 to − 6.85	0.96
	Non-linear	+ 157.8	+ 505.4	+ 0.42 to − 7.13	0.96
RFI-NCC-Xan	Linear	+ 176.4	+ 552.1	− 1.54 to − 6.69	0.89
	Non-linear	+ 185.7	+ 571.2	− 1.82 to − 7.01	0.92

elevated temperatures (RFI-C: − 0.01 to − 9.08 kJ mol^{-1}; RFI-NCC: + 0.70 to $^{-}$6.85 kJ mol^{-1}; RFI-RAW: − 0.46 to − 9.78 kJ mol^{-1}; RFI-NCC-Xan: − 1.54 to − 6.69 kJ mol^{-1}). Linear Van't Hoff analysis yielded positive ΔH° values (+ 107–185 kJ·mol^{-1}) for all sorbents, indicating endothermic uptake, while ΔS° values (+ 354–610 J mol^{-1} K^{-1}) confirmed substantial disorder and desolvation at the solid–liquid interface. Non-linear regression provided consistent trends but revealed slightly higher enthalpic contributions, particularly for RFI-C and RFI-NCC-Xan, suggesting stronger temperature dependence than inferred from linear fits Table 8. The combination of endothermicity and high entropy change demonstrates that adsorption is entropy-driven and becomes increasingly favorable at higher temperatures [78]. Among the materials, RFI-C exhibited the strongest thermodynamic driving force, while nanocellulose-based derivatives (RFI-NCC and RFI-NCC-Xan) showed enhanced spontaneity and more favorable molecular interactions compared with the raw biomass. Linear regression fits were highly reliable for RFI-C and RFI-NCC ($R^2 \geq 0.96$), whereas lower linearity observed in RFI-RAW and RFI-NCC-Xan indicated minor deviations from the idealized Van't Hoff model, consistent with the heterogeneity of adsorption sites.

8 .

9 Differentiating adsorption from photodegradation

Control experiments under UV (365 nm) and dark conditions confirmed adsorption as the dominant removal mechanism. Under UV, Atrazine degradation followed pseudo-first-order kinetics with a low-rate constant of $k = 0.003\ min^{-1}$, yielding a half-life of ~ 231 min. After 80 min, UV-induced degradation reached ~ 21% from 10.0 mg/L to 7.89 mg/L, while adsorption accounted for > 99% removal. These results align with findings by [68, 69], confirming Atrazine's low photolytic susceptibility and emphasizing (bio) sorption over (photo) degradation. Biosorbent particles may also shield Atrazine from UV, reducing degradation further.

10 Techno-economic evaluation

The valorization of *Raphia farinifera* inflorescence into biosorbents represents a low-cost alternative to conventional adsorbents such as activated carbon. Raw material sourcing from agricultural residues minimizes feedstock cost, while functionalization steps (acid hydrolysis, oxidation, and xanthation) remain relatively low in chemical and energy input compared with carbonization and activation processes. A preliminary cost estimate indicates that RFI-based adsorbents can be produced at less than one-third the cost of commercial activated carbon [79].The regeneration efficiency (> 80% after four cycles) further reduces replacement costs, extending material lifespan in continuous operation. Coupled with moderate adsorption capacities (8.6–9.4 mg g^{-1}), the cost per unit of contaminant removed is competitive with other biosorbent systems. Adoption at pilot scale in agricultural regions could therefore provide an economically viable and sustainable approach to Atrazine remediation.

11 Statistical analysis

All experimental results were obtained in triplicate, and data are presented as mean ± standard deviation. Kinetic and isotherm models were evaluated using non-linear regression, with goodness-of-fit assessed by correlation coefficients (R^2), chi-square (χ^2), and root mean square error (RMSE). One-way analysis of variance (ANOVA) confirmed significant differences ($p < 0.05$) in adsorption performance between biosorbents. Tukey's post hoc test further identified RFI-NCC-Xan as significantly more efficient than RFI-RAW and RFI-C, while not statistically different from RFI-NCC. These results validate the observed trends in adsorption capacity and confirm the reproducibility of the data.

12 Conclusion

This study demonstrated the potential of *Raphia farinifera* inflorescence as a renewable precursor for biosorbents applied to atrazine removal from aqueous systems. Four derivatives-RFI-RAW, RFI-C, RFI-NCC, and RFI-NCC-Xan exhibited distinct adsorption performances governed by their structural and surface chemical modifications. RFI-C achieved the highest Langmuir monolayer adsorption capacity ($q_m = 99.78$ mg/g), while RFI-NCC-Xan consistently provided superior removal efficiencies, attaining > 99% at pH 6, 0.4 g dosage, and 40 °C. Equilibrium was rapidly attained within 60–80 min, and kinetic evaluation confirmed the pseudo-second-order model as the most appropriate, with experimental and calculated adsorption capacities in strong agreement (q_e,exp = 9.82 mg/g; q_e,calc = 9.74 mg/g). Thermodynamic analysis verified the spontaneity of atrazine uptake, with ΔG° values between − 0.01 and − 9.78 kJ/mol. Positive enthalpy values (ΔH° = + 107–185 kJ/mol) established endothermic adsorption, complemented by large positive entropy changes (ΔS° = + 354–610 J·mol^{-1} K^{-1}), highlighting desolvation and increased interfacial disorder as dominant driving forces. Non-linear Van't Hoff regression reinforced these findings and indicated slightly stronger temperature dependence for RFI-C and RFI-NCC-Xan compared with linear estimates. Overall, adsorption was entropy-driven and became increasingly

favorable at higher temperatures. Regeneration tests indicated that RFI-NCC-Xan retained 81.59% removal efficiency after three NaOH desorption cycles, confirming operational stability and reusability. Application to field wastewater from rice farms in Aninri, Enugu State, Nigeria, yielded > 93% atrazine removal in both wet and dry seasons, demonstrating practical efficacy beyond controlled laboratory conditions. Collectively, these findings establish *Raphia farinifera*-derived biosorbents as low-cost, environmentally friendly, and efficient materials for herbicide remediation in agricultural settings, offering a sustainable alternative to conventional activated carbon.

Acknowledgements The authors gratefully acknowledge Engr. Agboeze Joseph Ogbonna for his valuable assistance in sourcing the Raphia farinifera inflorescence materials used in this study from Chief Joseph and Steller Agboeze farmland in Ajiona Mbu-Amon. His support in facilitating access to the study materials is sincerely appreciated.

Authors' contributions All authors contributed to the study conception and design. Material preparation, data collection and analysis were performed by E.A. The first draft of the manuscript was written by E.A and all authors commented on previous versions of the manuscript. All authors read and approved the final manuscript.

Funding This research did not receive any specific grant from funding agencies in the public, commercial, or not-for-profit sectors.

Data availability The datasets during and/or analyzed during the current study available from the corresponding author on reasonable request.

Declarations

Ethics approval and consent to participate Plant guidelines: The collection and use of *Raphia farinifera* inflorescence complied with local, national, and institutional guidelines governing the use of plant materials for research. All procedures adhered to the ethical standards of Enugu State University of Science and Technology (ESUT) and the National Environmental Standards and Regulations Enforcement Agency (NESREA) guidelines for non-endangered plant species. Permissions to collect the plants/plant parts: Permission for the collection of *Raphia farinifera* inflorescences was obtained from the local landowners and community authority in Mbu-Amon, Enugu State, Nigeria. As the species is cultivated and not endangered, no additional governmental license was required. Source of the plant used in the study: The *Raphia farinifera* inflorescences were sourced from cultivated plantations in Mbu-Amon, Isi-Uzo Local Government Area, Enugu State, Nigeria (coordinates: 6.71° N, 7.52° E). The species was identified and authenticated in the Department of Applied Biology and Biotechnology, ESUT, where a voucher specimen was deposited.

Consent for publication All authors have read and approved the final version of the manuscript.

Competing interests The authors declare no competing interests.

Open Access This article is licensed under a Creative Commons Attribution 4.0 International License, which permits use, sharing, adaptation, distribution and reproduction in any medium or format, as long as you give appropriate credit to the original author(s) and the source, provide a link to the Creative Commons licence, and indicate if changes were made. The images or other third party material in this article are included in the article's Creative Commons licence, unless indicated otherwise in a credit line to the material. If material is not included in the article's Creative Commons licence and your intended use is not permitted by statutory regulation or exceeds the permitted use, you will need to obtain permission directly from the copyright holder. To view a copy of this licence, visit http://creativecommons.org/licenses/by/4.0/.

References

1. Chukwudi-Madu E, Agboeze E, Chime CC, Nwadiogbu JO, Ajah N. Kinetic and equilibrium isotherm of pesticides (atrazine) adsorption unto activated carbon of calabash (lagenaria siceraria). EPRA Intern J Multidiscip Res. 2022;8(7):279–90.
2. Jablonowski ND, Schäffer A, Burauel P. Still present after all these years: persistence plus potential toxicity raise questions about the use of atrazine. Environ Sci Pollut Res. 2011;18(2):328–31.
3. Hayes TB, Anderson LL, Beasley VR, De Solla SR, Iguchi T, Ingraham H, et al. Demasculinization and feminization of male gonads by atrazine: consistent effects across vertebrate classes. J Steroid Biochem Mol Biol. 2011;273(1–2):64–73.
4. Zhao H, Qian H, Cui J, Ge Z, Shi J, Huo Y, et al. Endocrine toxicity of atrazine and its underlying mechanisms. Toxicology, 505, 153846. Toxicology. 2024;505:153846.
5. Agboeze E, Theresa O, Ogbobe O. Extraction and characterization of pharmaceutical grade microcrystalline cellulose from *Raphia farinifera* inflorescence. Univer J Pharm Res. 2022;7(4):59–67.
6. Kato S&KY. Comprehensive review of industrial wastewater treatment techniques. Environ Sci Pollut Res. 2024;31(39):51064–97.
7. Karić N, Maia AS, Teodorović A, Atanasova N, Langergraber G, Crini G, et al. Bio-waste valorisation: agricultural wastes as biosorbents for removal of (in) organic pollutants in wastewater treatment. Chem Eng J Adv. 2022;9:100239. https://doi.org/10.1016/j.ceja.2021.100239.

8. Baby R, Hussein MZ, Zainal Z, Abdullah AH. Preparation of functionalized palm kernel shell bio-adsorbent for the treatment of heavy metal-contaminated water. J Hazard Mater Adv. 2023;10:100253. https://doi.org/10.1016/j.hazadv.2023.100253.
9. Dehghani MH, Ahmadi S, Ghosh S, Khan MS, Othmani A, Khanday WA, et al. Sustainable remediation technologies for removal of pesticides as organic micro-pollutants from water environments: a review. Appl Surf Sci Adv. 2024;19:100558. https://doi.org/10.1016/j.apsadv.2023.100558.
10. Said G, Zahoor M, Moussa SB, Alzahrani AYA. Plant-based modified cellulose obtained from *Populus nigra* as a potential adsorbent for pesticides removal from aqueous media. Sci Rep. 2025;15(1):1–17.
11. Canton H. United Nations Environment Programme—UNEP. In: Canton H, editor. The Europa directory of international organizations 2021. Routledge: Oxfordshire; 2021. p. 188–214.
12. Camargos CH, Rezende CA. Structure–property relationships of cellulose nanocrystals and nanofibrils: implications for the design and performance of nanocomposites and all-nanocellulose systems. ACS Appl Nano Mater. 2021;4(10):10505–18.
13. Kumar S, Kumar A, Thakur A, Kumari P. Valorizing cellulosic biomass waste into valuable nano-biosorbents. In: Gupta A, Kumar R, Kumar V, editors. Integrated waste management. Singapore: Springer; 2024. p. 239–68.
14. Foo KY, Hameed BH. Detoxification of pesticide waste via activated carbon adsorption process. J Hazard Mater. 2010;175(1–3):1–11. https://doi.org/10.1016/j.jhazmat.2009.10.014.
15. Phan KA, Phihusut D, Tuntiwiwattanapun N. Preparation of rice husk hydrochar as an atrazine adsorbent: optimization, characterization, and adsorption mechanisms. J Environ Chem Eng. 2022;10(3):107575. https://doi.org/10.1016/j.jece.2022.107575.
16. Kuppusamy B, Gopalakrishnan S, Natesan S, Rajamohan N, Rajasimman M, Yusuf M, et al. alorization of sugarcane bagasse cellulose to synthesize novel graphene oxide-based composite for remediation of atrazine–Optimization studies. J Environ Chem Eng. 2024;12(3):112767. https://doi.org/10.1016/j.jece.2024.112767.
17. Wang D, Wang X, Song S, Hu K, Wu J, Chen Y. ZnCl2-modified almond shell-based biochar for highly efficient adsorption of crystal violet and methylene blue in water. Biomass Convers Biorefin. 2025. https://doi.org/10.1007/s13399-025-06739-7.
18. Reis DT, de-Aguiar Filho SQ, Grotto CGL, Bihain MFR, Pereira DH. Carboxymethylcellulose and cellulose xanthate matrices as potential adsorbent material for potentially toxic Cr 3+, Cu 2+ and Cd 2+ metal ions: a theoretical study. Theor Chem Acc. 2020;139:1–8.
19. Agboeze E, Uchechukwu Theresa O, Ogbobe O. Extraction and characterization of pharmaceutical grade microcrystalline cellulose from Raphia farinifera inflorescence. Univers J Pharm Res. 2022. https://doi.org/10.22270/ujpr.v7i4.816.
20. Rao LN, Lakavat M, Gandi S, Sri GK. Extraction and characterization of cellulose from agricultural waste materials. Mater Today: Proc. 2023. https://doi.org/10.1016/j.matpr.2021.07.030.
21. Getachew M, Gabriel T, Belete A, Gebre-Mariam T. Extraction and characterization of cellulose and microcrystalline cellulose from Teff straw and evaluation of the microcrystalline cellulose as tablet excipient. J Nat Fibers. 2023;20(2):2245565.
22. agboeze E, Ani N, Omeje E. Extraction and characterization of pharmaceutical grade microcrystalline cellulose from Bambara nut (*Voandzeia subterranean* (L) Thousars) husk. Afr Sci Rep. 2022;1(2):103–14.
23. Das L, Saha N, Saha PD, Bhowal A, Bhattacharya C. Application of synthesized nanocellulose material for removal of malachite green from wastewater. In: Ghosh S, Saha P, Di Francesco M, editors. Recent trends in waste water treatment and water resource management. Singapore: Springer; 2020. p. 11–22.
24. Thommes M, Kaneko K, Neimark AV, Olivier JP, Rodriguez-Reinoso F, Rouquerol J, et al. Physisorption of gases, with special reference to the evaluation of surface area and pore size distribution (IUPAC technical report). Pure Appl Chem. 2015;87(9–11):1051–69.
25. Lagergren S. Zur Theorie der Sogenannten Adsorption Gelöster Stoffe. Kungliga Svenska Vetenskapsakademiens Handlingar. 1898;24(4):1–39.
26. Ho Y, McKay G. Pseudo-second order model for sorption processes. Process Biochem. 1999;34(5):451–65.
27. Foo K, Hameed B. Insights into the modeling of adsorption isotherm systems. Chem Eng J. 2010;156(1):2–10.
28. Steiger BG, Zhou Z, Anisimov YA, Evitts RW, Wilson LD. Valorization of agro-waste biomass as composite adsorbents for sustainable wastewater treatment. Ind Crops Prod. 2023;191:115913. https://doi.org/10.1016/j.indcrop.2022.115913.
29. Cuong TD, Hoang PH. Preparation of bio-based porous material with high oil adsorption capacity from bio-polyurethane and sugarcane bagasse. RSC Adv. 2024;14(10):6938–47.
30. Sireesha S, Sreedhar I. Holistic and parametric optimization study on Cr (VI) removal using acid-treated coco peat biochar adsorbent. Bioresour Technol Rep. 2023;22:101486.
31. Tsai WT, Hsu CH, Lin YQ, Tsai CH, Chen WS, Chang YT. Enhancing the pore properties and adsorption performance of cocoa pod husk (CPH)-derived biochars via post-acid treatment. Processes. 2020;8(2):44. https://doi.org/10.3390/pr8020144.
32. Hussain MAAS, Kousar T, Mahmood F, Haruna A, Zango ZU, Keshta BE. Efficient removal of manganese (II) ions from aqueous solution using biosorbent derived from rice husk. Sustain Chem One World. 2025;5:100047.
33. Singh S, Kumar V, Datta S, Dhanjal DS, Sharma K, Samuel J, et al. Current advancement and future prospect of biosorbents for bioremediation. Sci Total Environ. 2020;709:135895. https://doi.org/10.1016/j.scitotenv.2019.135895.
34. Geetha T, Smitha JK, Sebastian M, Litty MI, Joseph B, Joseph J, et al. Synthesis and characterization of nano iron oxide biochar composite for efficient removal of crystal violet from water. Heliyon. 2024;10(21):e39450. https://doi.org/10.1016/j.heliyon.2024.e39450.
35. Ibitoye SE, Loha C, Mahamood RM, Jen TC, Alam M, Sarkar I, et al. An overview of biochar production techniques and application in iron and steel industries. Bioresour Bioprocess. 2024;11(1):65.
36. El Messaoudi N, Ulfa M, Hamzah A, Hamid ZAA, Ramadhani DV, Suryanegara L, et al. Fabrication a sustainable adsorbent nanocellulose-mesoporous hectorite bead for methylene blue adsorption. Case Stud Chem Environ Eng. 2024;10:100850.
37. Hayawin ZN, Ibrahim MF, Faizah JN, Ropandi M, Astimar AA, Noorshamsiana AW, et al. Palm oil mill final discharge treatment by a continuous adsorption system using oil palm kernel shell activated carbon produced from two-in-one carbonization activation reactor system. J Water Process Eng. 2020;36:101262.
38. Adebowale KO, Egbedina AO. Facile green synthesis of bio-carbon material from eggshells and its application for the removal of bisphenol A and 2, 4, 6-trichlorophenol from water. Environ Nanotechnol, Monit Manag. 2022;17:100622. https://doi.org/10.1016/j.enmm.2021.100622.

39. Baksi S, Saha D, Saha S, Sarkar U, Basu D, Kuniyal JC. Pre-treatment of lignocellulosic biomass: review of various physico-chemical and biological methods influencing the extent of biomass depolymerization. Int J Environ Sci Technol. 2023;20(12):13895–922.
40. Omokafe SM, Adeniyi AA, Igbafen EO, Oke SR, Olubambi PA. Fabrication of activated carbon from coconut shells and its electrochemical properties for supercapacitors. Int J Electrochem Sci. 2020;15(11):10854–65.
41. Umeh CT, Nduka JK, Iwuozor OK, Omokpariola OD, Dulta K, Ezeh SC, et al. Adsorption modelling on the removal of ciprofloxacin antibiotic from aqueous solution by acid-modified corn cob. Int J Environ Anal Chem. 2025;105(2):432–57.
42. Agboeze E, Uchechukwu TO, Ogbobe O. Novel Strong And Weak Kola Nut (Cola-Sterculiaceae) Testa Cation Exchangers For The Remediation Of Polluted Water. Am J Innov Res Appl Sci. 2020;11(1):13–5.
43. Vu N, Nguyen LH, Tran HCV, Yoshimura K, Tran TD, Van Le H, et al. Cellulose nanocrystals extracted from rice husk using the formic/peroxyformic acid process: isolation and structural characterization. RSC Adv. 2024;14(3):2048–60.
44. Noremylia MB, Hassan MZ, Ismail Z. Recent advancement in isolation, processing, characterization and applications of emerging nanocellulose: a review. Int J Biol Macromol. 2022;206:954–76.
45. Abou Dib M, Gore E, Grisel M. Intrinsic and rheological properties of hydrophobically modified xanthan synthesized under green conditions. Food Hydrocoll. 2023;138:108461.
46. Pin TC, Nascimento VM, Costa AC, Pu Y, Ragauskas AJ, Rabelo SC. Structural characterization of sugarcane lignins extracted from different protic ionic liquid pretreatments. Renew Energy. 2020;161:579–92.
47. Joshi SK, Bhandari NS. Estimation of sorption–desorption characteristics of biosorbent of Lantana camara leaves for removal of Pb (II) ions from wastewater. Environ Monit Assess. 2023;195(1):42.
48. Onokwai O, Ajisegiri ESA, Okokpujie IP, Ibikunle RA, Oki M, Dirisu JO. Characterization of lignocellulose biomass based on proximate, ultimate, structural composition, and thermal analysis. Mater Today: Proc. 2022;65:2156–62.
49. Rasheed HA, Adeleke AA, Nzerem P, Olosho AI, Ogedengbe TS, Jesuloluwa S. Isolation, characterization and response surface method optimization of cellulose from hybridized agricultural wastes. Sci Rep. 2024;14(1):14310.
50. Xiao R, Yang W, Cong X, Dong K, Xu J, Wang D, et al. Thermogravimetric analysis and reaction kinetics of lignocellulosic biomass pyrolysis. Energy. 2020;201:117537. https://doi.org/10.1016/j.energy.2020.117537.
51. Kursunoglu S, Demir I. The potential of pistachio shell-based activated carbons for metal removal from aqueous solutions: a review. Energy Sources Part A Recover Util Environ Eff. 2022;44(4):8572–90.
52. Negi S, Joshi SK, Bhandari NS. Biosorption of zinc on functionally activated Lantana camara leaves: equilibrium, kinetic, and thermodynamic studies. Biomas Convers Biorefinery. 2024;15:24117–34.
53. Djekoune L, Maaliou A, Salem Z, Ziani D, Kamel R, Ouakouak A, et al. Phosphate adsorption on dried alum sludge: modeling and application to treatment of dairy effluents. Environ Res. 2024;252:118976. https://doi.org/10.1016/j.envres.2024.118976.
54. Wang Q, Xiao Y, Qi J, Wei H, Zhao J, Lei X, et al. A novel strategy for preparing porous Fe/Ca-loaded biochar transformed from municipal sludge towards phosphate removal. J Water Process Eng. 2024;66:106109.
55. Wang S, Sun J, Wang Y. Sulfur-functionalized biochar for enhanced removal of pesticides from water. Bioresour Technol. 2019;282:94–101.
56. Gupta K, Carrott PJM, Ribeiro Carrott MML. Low-cost adsorbents: growing approach to wastewater treatment—a review. Crit Rev in Environ Sci Technol. 2009;38(10):783–842.
57. Siddiqui U, Ilyas RA, Sapuan SM, Ab Hamid NH, Khoo PS, Chowdhury A, et al. Alginate-based materials as adsorbent for sustainable water treatment. Intern J Biol Macromol. 2025;298:139946.
58. Lartey-Young G, Ma L. Optimization, equilibrium, adsorption behaviour of Cu/Zn/Fe LDH and LDHBC composites towards atrazine reclamation in an aqueous environment. Chemosphere. 2022;293:133526.
59. Algieri A, Tursi P, Costanzo L, Maiuolo AD, Nino AN, Beneduci A. Thiol-functionalized cellulose for mercury polluted water remediation: Synthesis and study of the adsorption properties. Chemosphere. 2024;355:141891.
60. Dong L, Shan C, Liu Y, Sun H, Yao B, Gong G, et al. Characterization and mechanistic study of heavy metal adsorption by facile synthesized magnetic xanthate-modified chitosan/polyacrylic acid hydrogels. Int J Environ Res Public Health. 2022;19(17):11123.
61. Juliana J, Jesintha KL, Mariaamalraj S, Padmanaban VC, Neelakandan AR, Rajanikant GK. Biopolymers as a sustainable approach for wastewater treatment. In: Sustainable technologies for water and wastewater treatment. CRC Press; 2021. p. 259–74.
62. Ortiz-Martínez M, Restori-Corona B, Hernández-García L, Alonso-Segura D. Polysaccharides and composite adsorbents in the spotlight for effective agrochemical residue removal from water. Macromol. 2024;4(4):785–804.
63. Pishdadi-Aghdarreh F, Norouzbeigi R, Velayi E. Simultaneous adsorption of methylene blue cationic dye and paraquat herbicide on activated lightweight expanded clay aggregate (LECA) as a sustainable and recyclable adsorbent. Appl Clay Sci. 2024;256:107432. https://doi.org/10.1016/j.clay.2024.107432.
64. Kizito S, Wu S, Kirui WK, Lei M, Lu Q, Bah H, et al. Evaluation of slow pyrolyzed wood and rice husks biochar for adsorption of ammonium nitrogen from piggery manure anaerobic digestate slurry. Sci Total Environ. 2017;505:102–12.
65. Agboeze E, Chime C, Udeozo P, Ofordile V, Nsude O, Eze C, et al. Heavy metal contamination and health risks from dumpsite effluents in Enugu State Southeastern Nigeria. Environ Anal Health Toxicol. 2025;40(3):1–13.
66. Garba ZN, Abdullahi AK, Haruna A, Gana SAA. Risk assessment and the adsorptive removal of some pesticides from synthetic wastewater: a review. Beni-Suef Univ J Basic Appl Sci. 2021;10(1):19.
67. Mikolajczyk P, Fortela DLB, Berry JC, Chirdon WM, Hernandez RA, Gang DD, et al. Evaluating the suitability of linear and nonlinear regression approaches for the Langmuir adsorption model as applied toward biomass-based adsorbents: testing residuals and assessing model validity. Langmuir. 2024;40(39):20428–42.
68. France HE, Strong OL, Roy TM, Vreugdenhil AJ. Versatile waste wood-chitosan composites for 2, 4-D and paraquat adsorption: isotherm modelling and thermodynamic evaluation. Chemosphere. 2025;370:144008. https://doi.org/10.1016/j.chemosphere.2024.144008.
69. Dehghani MH, Hassani AH, Karri RR, Younesi B, Shayeghi M, Salari M, et al. Process optimization and enhancement of pesticide adsorption by porous adsorbents by regression analysis and parametric modelling. Sci Rep. 2021;11(1):11719.
70. Li P, Fang J, Huang D, Tang J, Huang J, Meng F. A low-cost and effective bagasse-based magnetic porous biochar as an adsorbent for solid phase extraction of triazine herbicides in brown sugar. Anal Methods. 2021;13(32):3585–91.

71. Thamarai P, Deivayanai VC, Swaminaathan P, Karishma S, Vickram AS, Yaashikaa PR. Experimental investigation of Cd (II) ion adsorption on surface-modified mixed seaweed biosorbent: a study on analytical interpretation and thermodynamics. Environ Res. 2024;260:119670.
72. Liu D, Liu Y, He H, Liu J, Yang X, Zhang L, et al. Functional bimetal/carbon composites Co/Zr@ AC for pesticide atrazine removal from water. Molecules. 2023;28(5):2071.
73. Stavra E, Petrou PS, Koukouvinos G, Kiritsis C, Pirmettis I, Papadopoulos M, et al. Simultaneous determination of paraquat and atrazine in water samples with a white light reflectance spectroscopy biosensor. J Hazard Mater. 2018;359:67–75.
74. Tao Y, Hu S, Han S, Shi H, Yang Y, Li H, et al. Efficient removal of atrazine by iron-modified biochar loaded *Acinetobacter lwoffii* DNS32. Sci Total Environ. 2019;682:59–69.
75. Lu H, Wang X, Cong Q, Chen X, Li Q, Li XYB. Research progress on the degradation of organic pollutants in water by activated persulfate using biochar-loaded nano zero-valent iron. Molecules. 2024;29(5):1130. https://doi.org/10.3390/molecules29051130.
76. Liang Y, Zhao B, Yuan C. Adsorption of atrazine by Fe-Mn-modified biochar: the dominant mechanism of π–π interaction and pore structure. Agronomy. 2022;12(12):3097.
77. Salamanca M, Lopez-Serna R, Palacio L, Hernández A, Prádanos P, Pena M. Study of the rejection of contaminants of emerging concern by a biomimetic aquaporin hollow fiber forward osmosis membrane. J Water Process Eng. 2021;40:101914.
78. Uzosike O, Ofudje EA, Akiode OK, Ikenna CV, Adeogun AI, Akinyele JO, et al. Magnetic supported activated carbon obtained from walnut shells for bisphenol-a uptake from aqueous solution. Appl Water Sci. 2022;12(8):201. https://doi.org/10.1007/s13201-022-01724-1.
79. Akpinar RJ, Drout T, Islamoglu S, Kato JL, Farha OK. Exploiting π–π interactions to design an efficient sorbent for atrazine removal from water. ACS Appl Mater Interfac. 2019;11(6):6097–103.
80. Liu R, Xie Y, Cui K, Xie J, Zhang Y, Huang Y. Adsorption behavior and adsorption mechanism of glyphosate in water by amino-MIL-101 (Fe). J Phys Chem Solids. 2022;161:110403. https://doi.org/10.1016/j.jpcs.2021.110403.
81. Hellal H, Abdelsalam WT, Ibrahim MA. Removal of atrazine from contaminated water by functionalized graphene quantum dots. Opt Quantum Electron. 2024;56(3):374.
82. Li Y, Yang X, Wong M, Geng B. Atrazine biodegradation in water by co-immobilized *Citricoccus* sp. strain TT3 with *Chlorella vulgaris* under a harsh environment. Algal Res. 2023;70:102994. https://doi.org/10.1016/j.algal.2023.102994.
83. Herrera-Gallardo E, Guzmán-Gil R, Colín-Luna JA, García-Martínez JC, León-Santiesteban HH, González-Brambila OM, et al. Atrazine biodegradation in soil by *Aspergillus niger*. Can J Chem Eng. 2021;99(4):932–46.
84. Farias C, Guimarães RC, Oliveira KR, Nazário CE, Ferencz JA, Wender H. Banana peel powder biosorbent for removal of hazardous organic pollutants from wastewater. Toxics. 2023;11(8):664.
85. Wang Y, Chen Y, Wang L, Mo Y, Lin X, Gao S, et al. Efficient removal of atrazine in wastewater by washed peanut shells biochar: adsorption behavior and biodegradation. Process Biochem. 2025;154:22–34.

Publisher's Note Springer Nature remains neutral with regard to jurisdictional claims in published maps and institutional affiliations.